ARTICLE

Design and synthesis of copper(II) and nickel(II) complexes as potential inhibitors against SARS-CoV-2 viral RNA binding protein and Omicron RBD protein

Reyaz Ahmad[a], Mukesh Choudhary[a]*

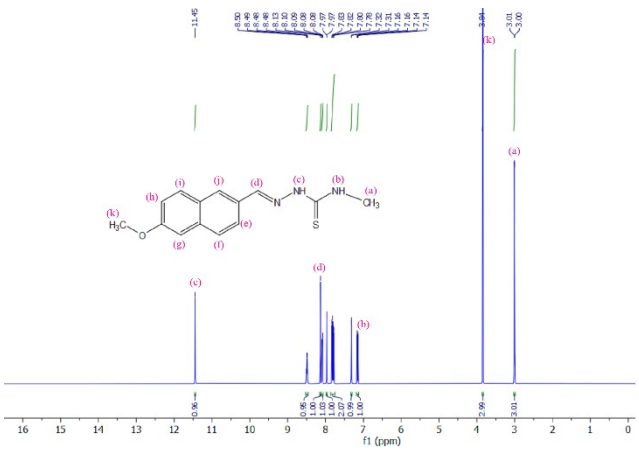

Figure S1. ^{1}H-NMR spectra of Schiff base ligand (L) in DMSO-d6 solution.

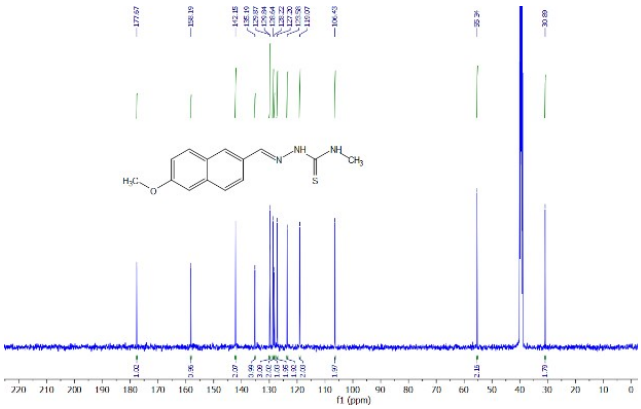

Figure S2. ^{13}C-NMR spectra of Schiff base ligand (L) in DMSO-d6 solution.

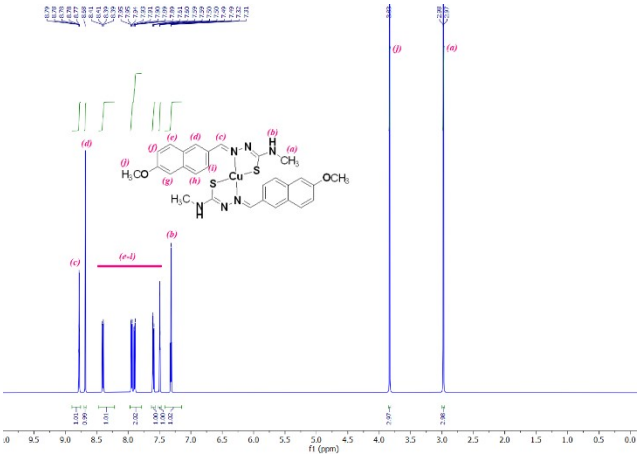

Figure S3. ^{1}H-NMR spectra of copper(II) complex $[Cu(L)_2]$(**1**) in DMSO-d6 solution.

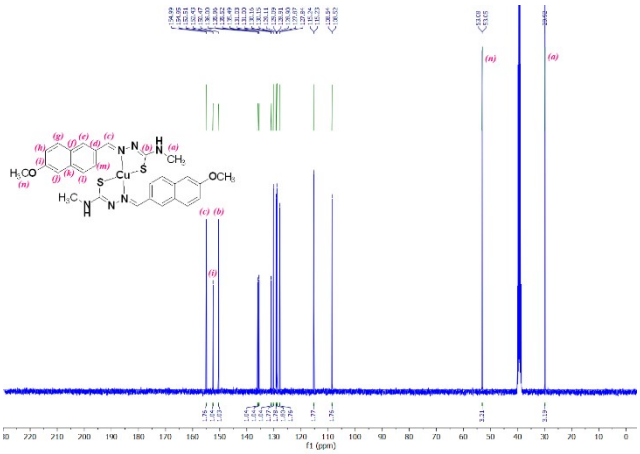

Figure S4. ^{13}C-NMR spectra of copper(II) complex $[Cu(L)_2]$(**1**) in DMSO-d6 solution.

[a] *Department of Chemistry, National Institute of Technology Patna, Patna-800005 (Bihar) India.*

[a.] *Corresponding author: mukesh@nitp.ac.in*

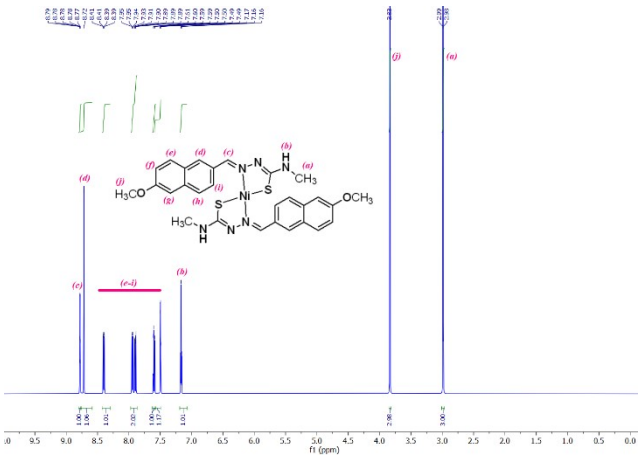

Figure S5. ^{1}H-NMR spectra of nickel(II) complex $[Ni(L)_2]$(**2**) in DMSO-d6 solution.

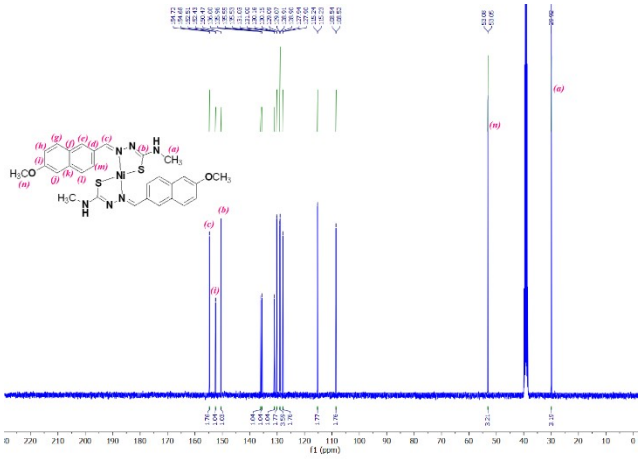

Figure S6. ^{13}C-NMR spectra of nickel(II) complex $[Ni(L)_2]$(**2**) in DMSO-d6 solution.

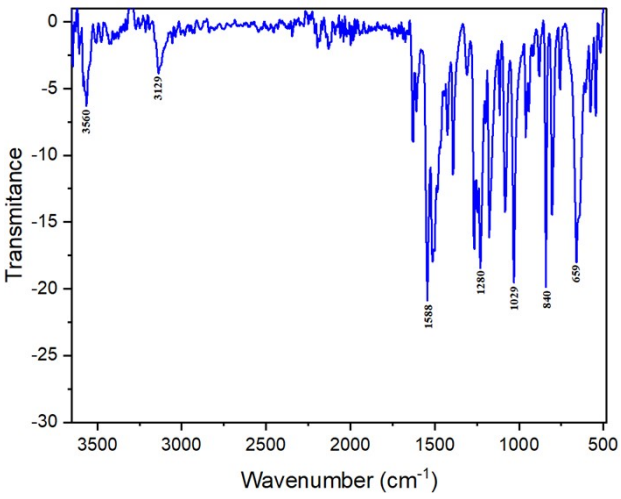

Figure S7. FT-IR spectra of Schiff base ligand (HL).

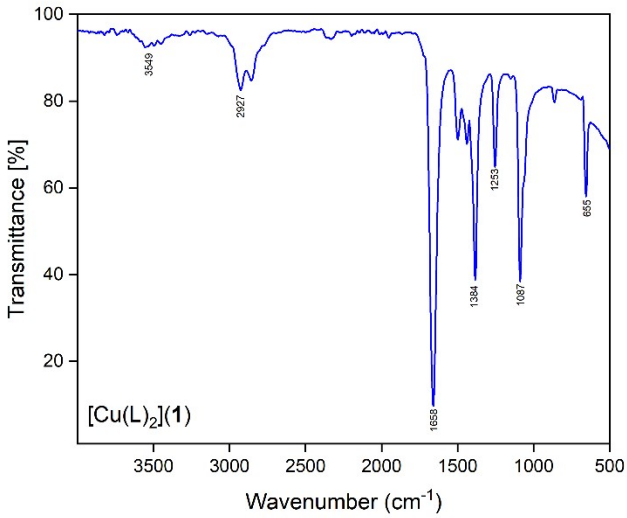

Figure S8. FT-IR spectra of copper(II) complex $[Cu(L)_2]$(**1**).

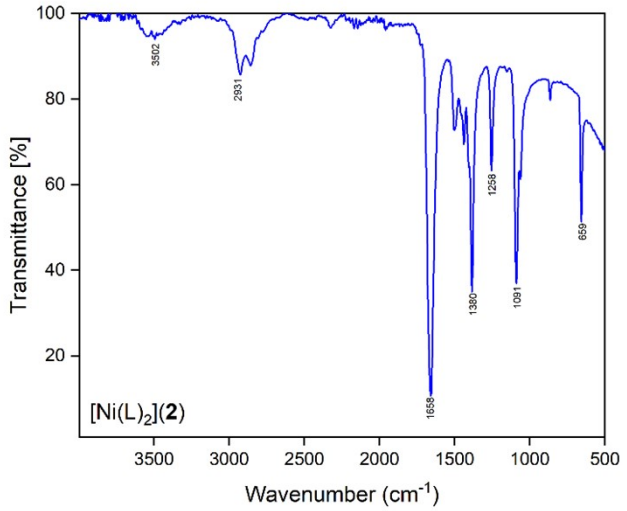

Figure S9. FT-IR spectra of nickel(II) complex $[Ni(L)_2]$(**2**).

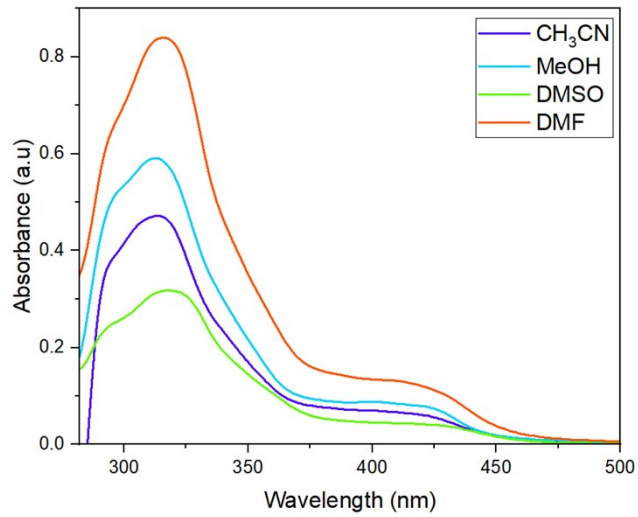

Figure S10. UV-Vis spectrum of copper(II) complex $[Cu(L)_2]$(**1**) in different solvents at room temperature..

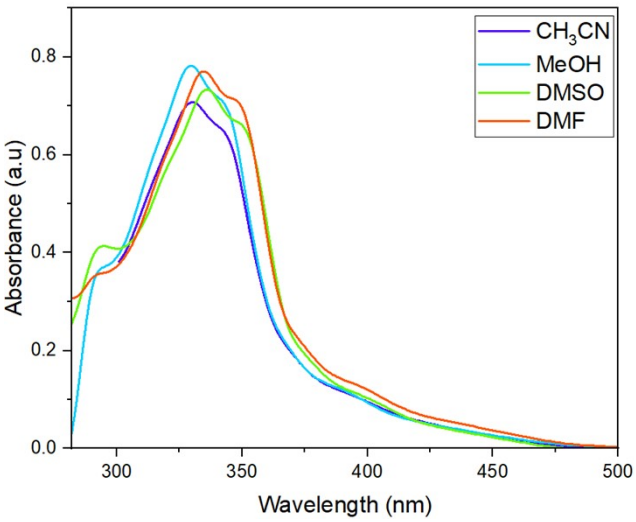

Figure S11. UV-Vis spectrum of nickel(II) complex $[Ni(L)_2]$(**2**) in different solvents at room temperature.

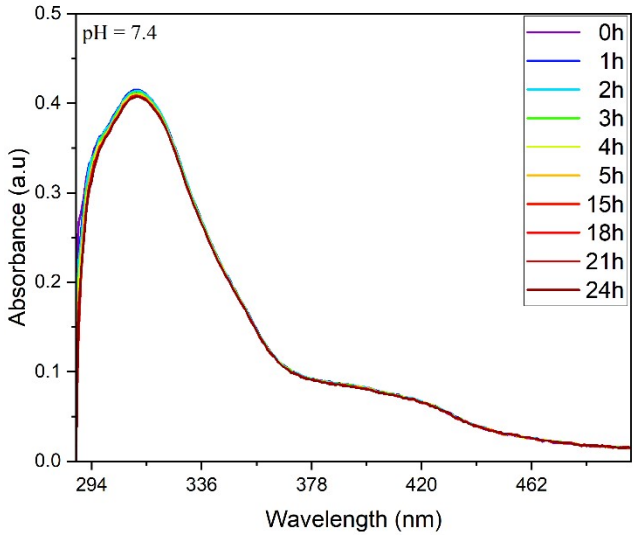

Figure S12. Time dependent absorption spectra of copper(II) complex $[Cu(L)_2]$(**1**) in buffer solution. [Inset: the expanded region depicting the stability of the complex in buffer medium]

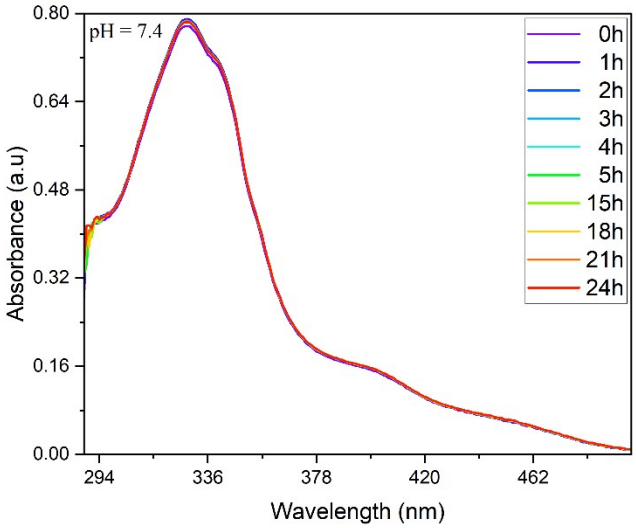

Figure S13. Time dependent absorption spectra of nickel(II) complex $[Ni(L)_2]$(**2**) in buffer solution. [Inset: the expanded region depicting the stability of the complex in buffer medium].

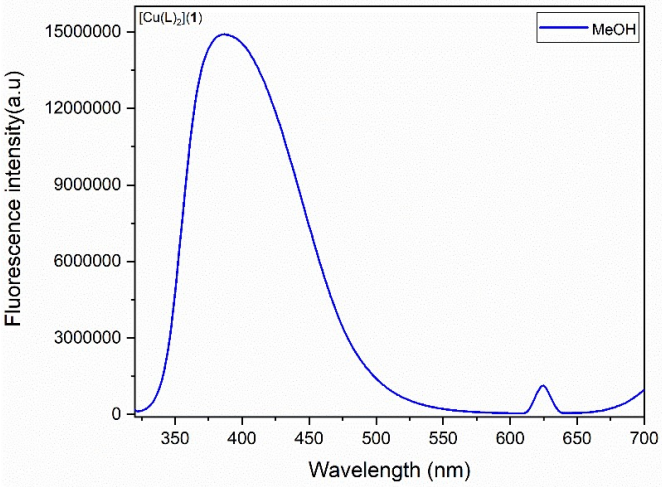

Figure S14. Fluorescence spectra of copper(II) complex $[Cu(L)_2]$(**1**) at room temperature.

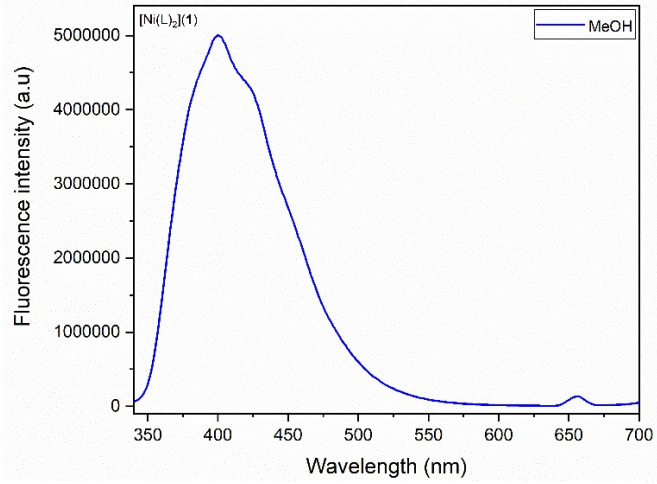

Figure S15. Fluorescence spectra of nickel(II) complex $[Ni(L)_2]$(**2**) at room temperature.

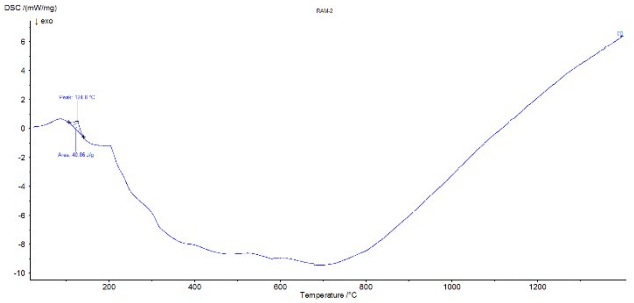

Figure S16. DSC thermal analysis of the copper(II) complex $[Cu(L)_2]$(**1**).

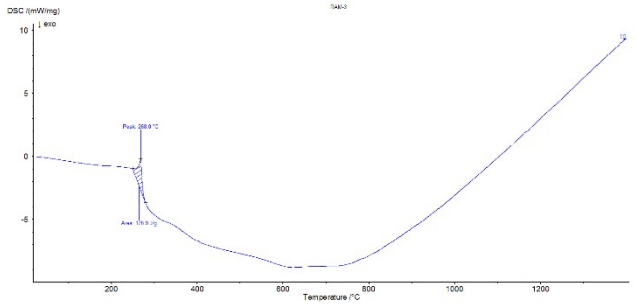

Figure S17. DSC thermal analysis of the nickel(II) complex $[Ni(L)_2]$(**2**).

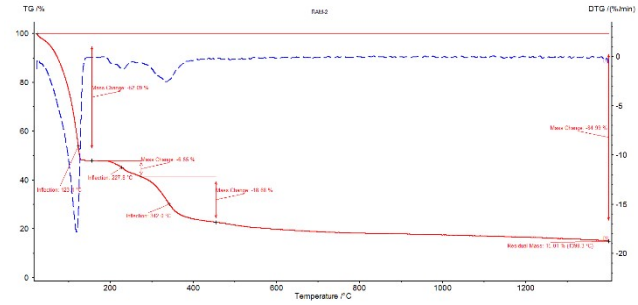

Figure S18.TG-DTG thermal analysis of the copper(II) complex $[Cu(L)_2]$(**1**).

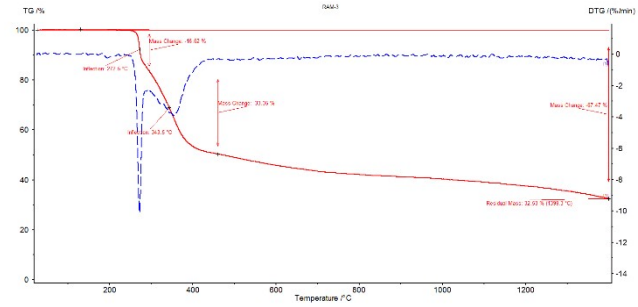

Figure S19. TG-DTG thermal analysis of the nickel(II) complex $[Ni(L)_2]$(**2**).

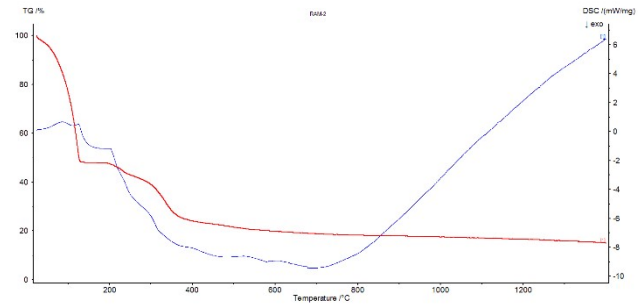

Figure S20. TG-DSC thermal analysis of the copper(II) complex $[Cu(L)_2]$(**1**).

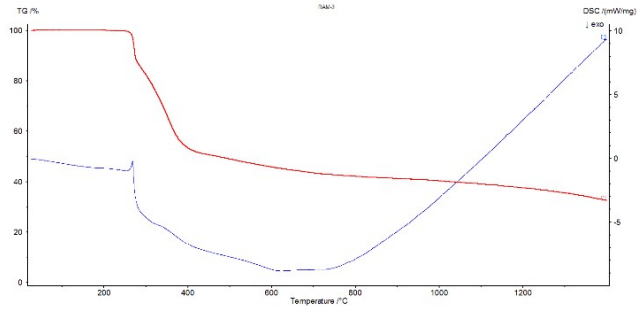

Figure S21. TG-DSC thermal analysis of the nickel(II) complex $[Ni(L)_2]$(**2**).

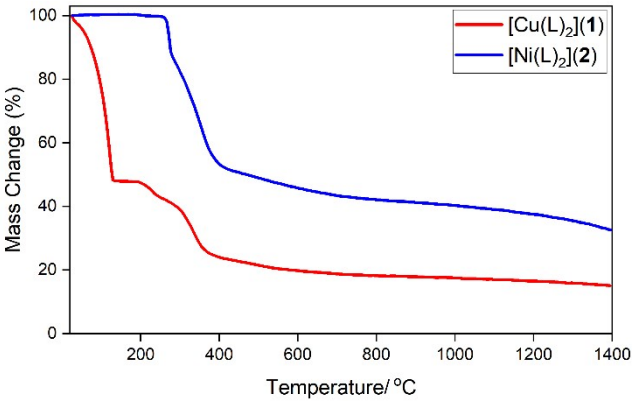

Figure S22. Mass loss comparison plots of the copper(II) complex $[Cu(L)_2]$(**1**) and nickel(II) complex $[Ni(L)_2]$(**2**).

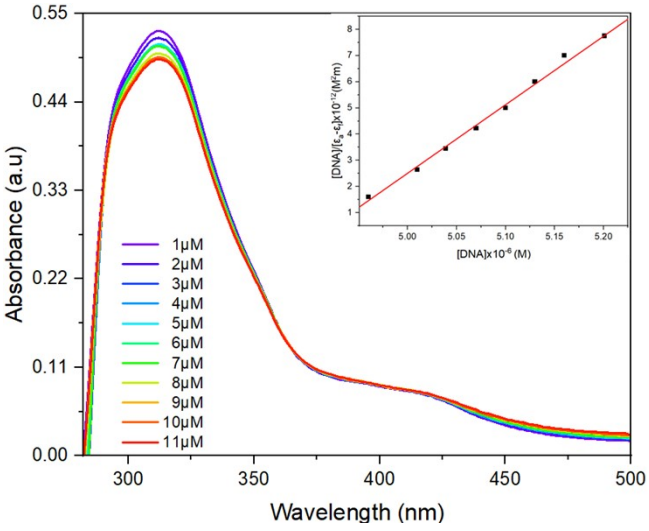

Figure S23. Absorption titration spectra of the copper(II) complex $[Cu(L)_2]$(**1**) upon incremental addition of CT-DNA [Inset: the linear fitting to determine binding constant].

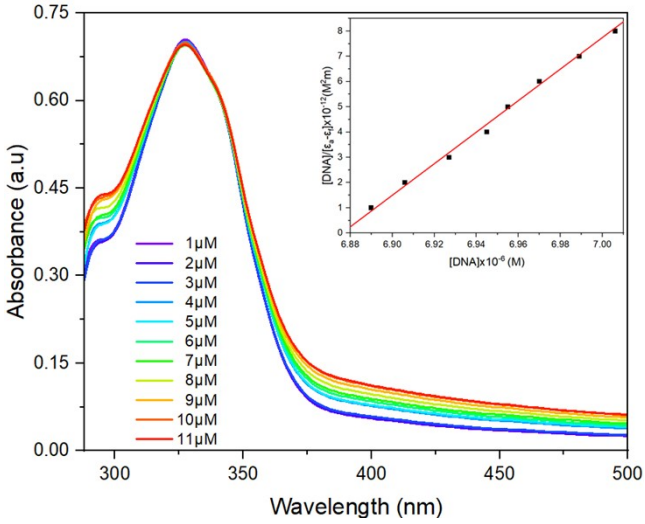

Figure S24. Absorption titration spectra of the nickel(II) complex $[Ni(L)_2]$(**2**) upon incremental addition of CT-DNA [Inset: the linear fitting to determine binding constant].

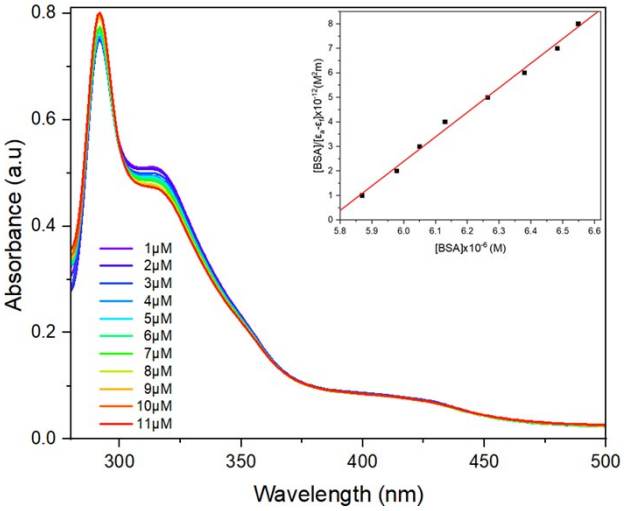

Figure S25. Absorption titration spectra of the copper(II) complex $[Cu(L)_2]$(**1**) upon incremental addition of BSA [Inset: the linear fitting to determine binding constant].

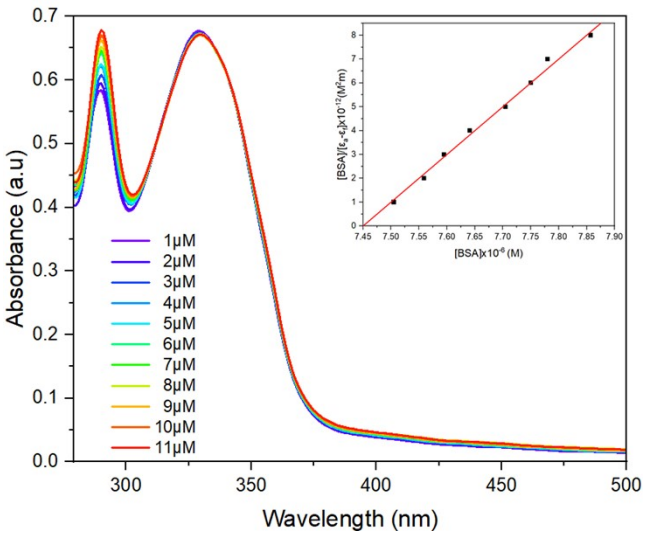

Figure S26. Absorption titration spectra of the nickel(II) complex $[Ni(L)_2]$(**2**) upon incremental addition of BSA [Inset: the linear fitting to determine binding constant].

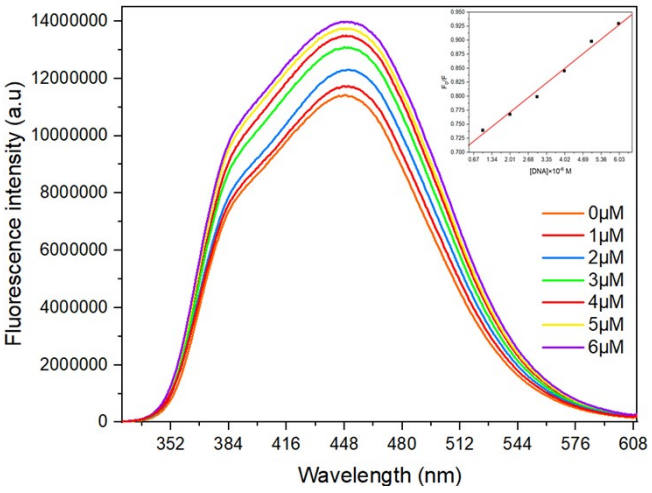

Figure S27. Emission titration spectra of the copper(II) complex $[Cu(L)_2]$(**1**) upon incremental addition of CT-DNA [Inset: the linear fitting to determine binding constant].

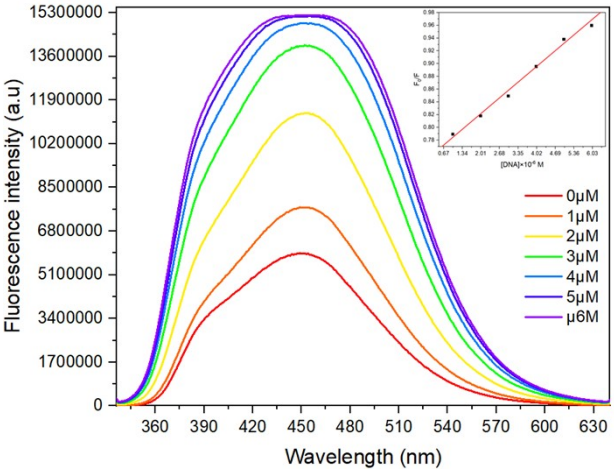

Figure S28. Emission titration spectra of the nickel(II) complex $[Ni(L)_2]$(**2**) upon incremental addition of calf-thymus DNA(CT-DNA) [Inset: the linear fitting to determine binding constant].

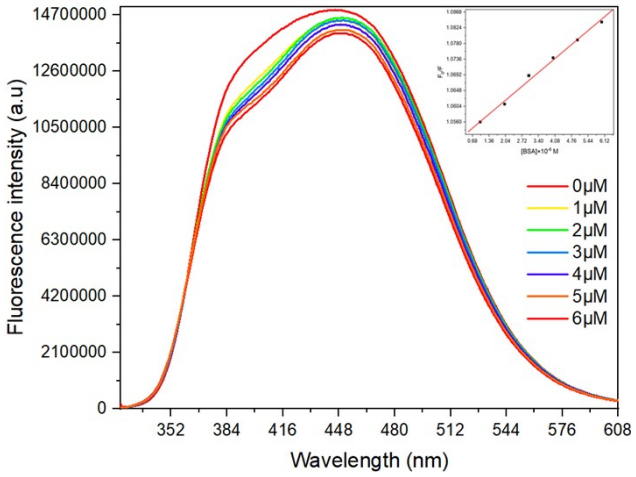

Figure S29. Emission titration spectra of the copper(II) complex $[Cu(L)_2]$(**1**) upon incremental addition of bovine serum albumin (BSA) [Inset: the linear fitting to determine binding constant].

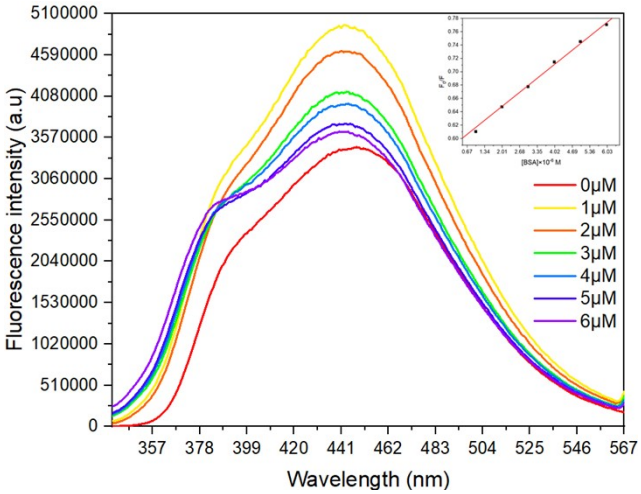

Figure S30. Emission titration spectra of the nickel(II) complex $[Ni(L)_2]$(**2**) upon incremental addition of BSA [Inset: the linear fitting to determine binding constant].

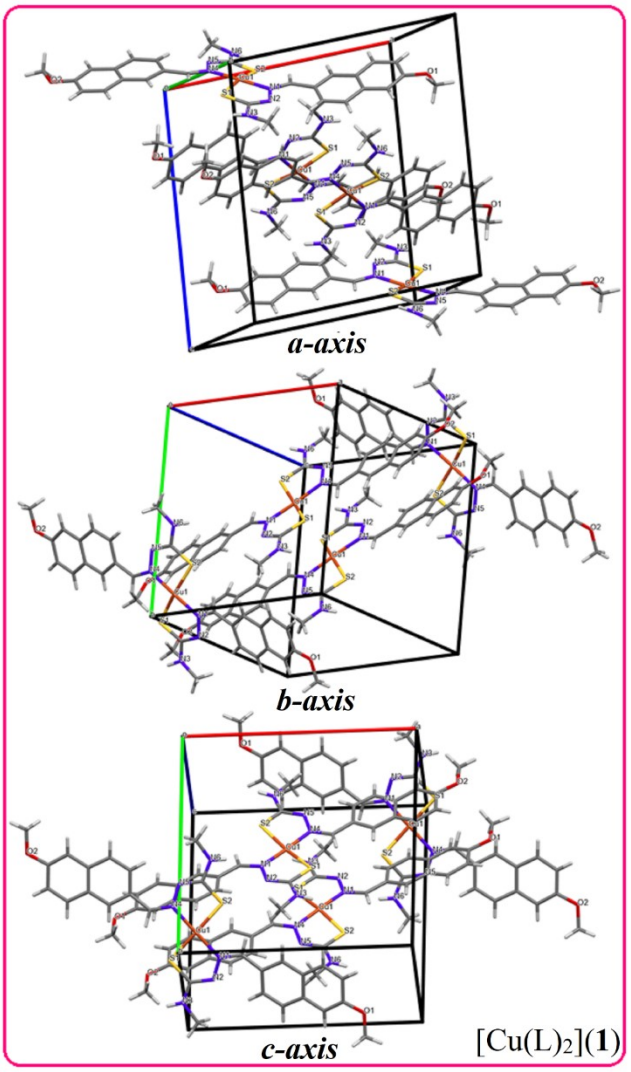

Figure S31. The packing view of bis-Schiff base copper(II) complex $[Cu(L)_2]$ (**1**) (along *a-c axis*).

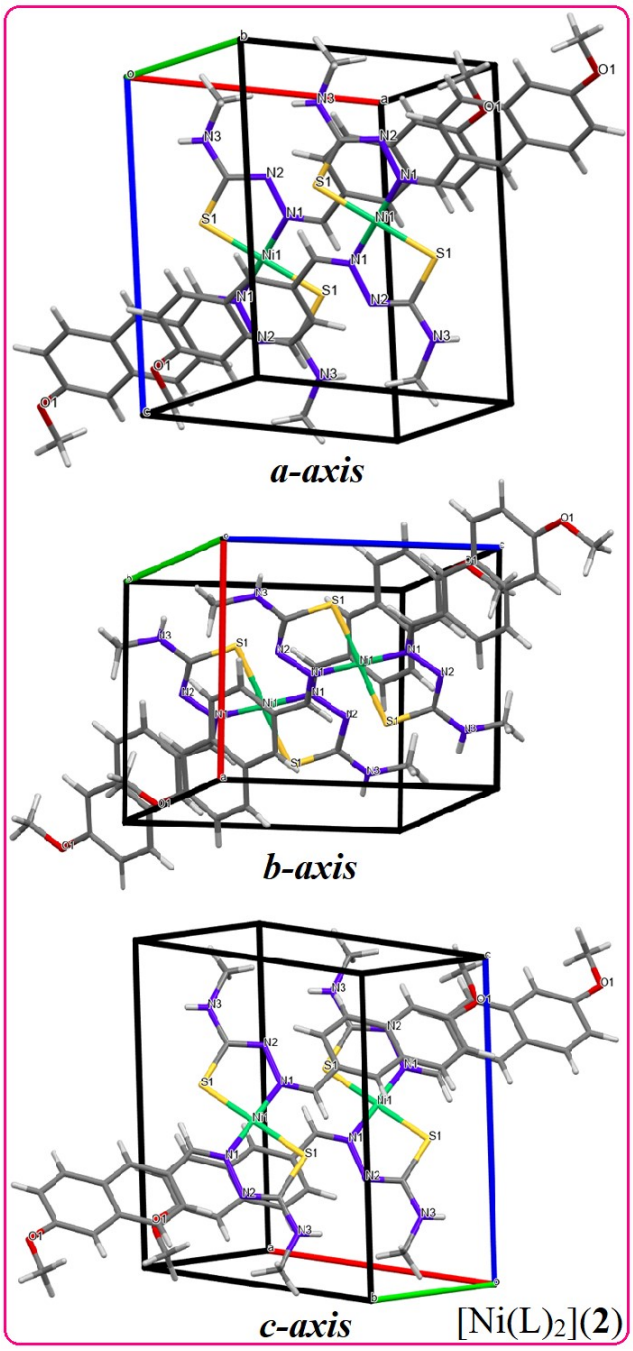

Figure S32. The packing view of bis-Schiff base nickel(II) complex $[Ni(L)_2]$(**2**) (along *a-c axis*).

Experiments exposure time and scan width

For the copper(II) complex $[Cu(L)_2]$(**1**), the data collection was performed at 100 (2) K with an exposure time of maximum 60 s for reflection (Omega scans; scan width: (1.10+0.15 tanθ)° ±25% to each side of the reflection to determine the background). The mean I/σ(I) is 7.1, and R_{int} is 22.33% for the structure of this complex (Figure S33 and S34). The effective resolution is only around 40 ° in 2θ, at which point R_{int} becomes larger than 30%. The data set that we have consists of very weak reflections and we have mentioned the poor quality of the crystal in the checkcif for the alerts, therefore this structure shows highly inconsistent data. After several attempts, we did not obtain good diffraction data for this structure. A representative structural drawing showing anisotropic displacement parameters (ADPs) of each structure is presented in Figure 4 and Figure S35, while summary of ADPs for copper(II) complex $[Cu(L)_2]$ (**1**) and nickel(II) complex $[Ni(L)_2]$(**2**) is tabulated in Table S6. From these ADPs images (fraction of atoms vs anisotropy), any disorder in each structure can be visualized and the nature of the actual molecule may be easily discernible for both the structures of copper(II) complex $[Cu(L)_2]$ (**1**) and nickel(II) complex $[Ni(L)_2]$(**2**).

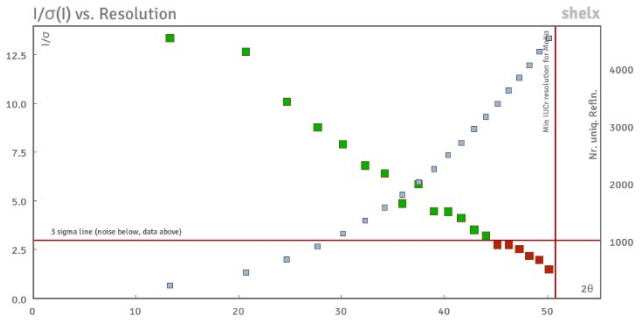

Figure S33. Diffraction data and refinement plot of copper(II) complex $[Cu(L)_2]$ (**1**) with I/σ(I) vs resolution.

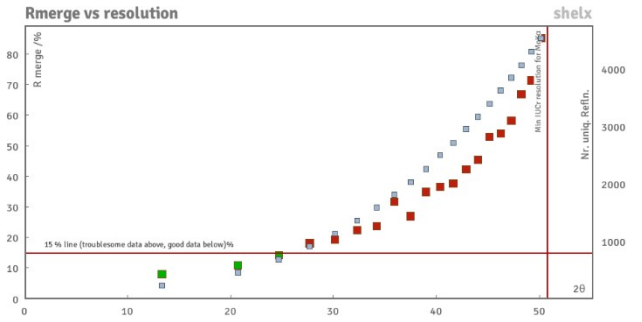

Figure S34. Diffraction data and refinement plot of copper(II) complex $[Cu(L)_2]$ (**1**) with R_{merge} vs resolution.

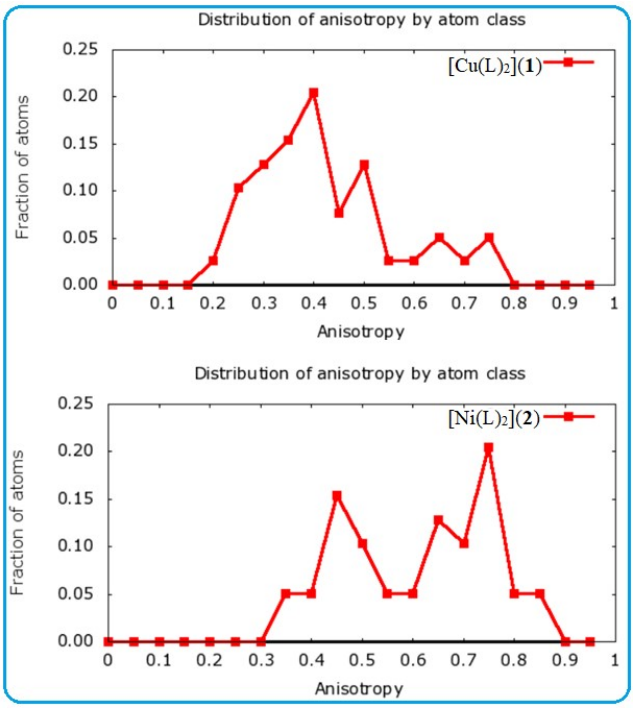

Figure S35. Graphical view of anisotropic displacement parameters (ADPs, Å^2 x 10^3) plot of copper(II) complex [Cu(L)$_2$] (**1**) and nickel(II) complex [Ni(L)$_2$](**2**).

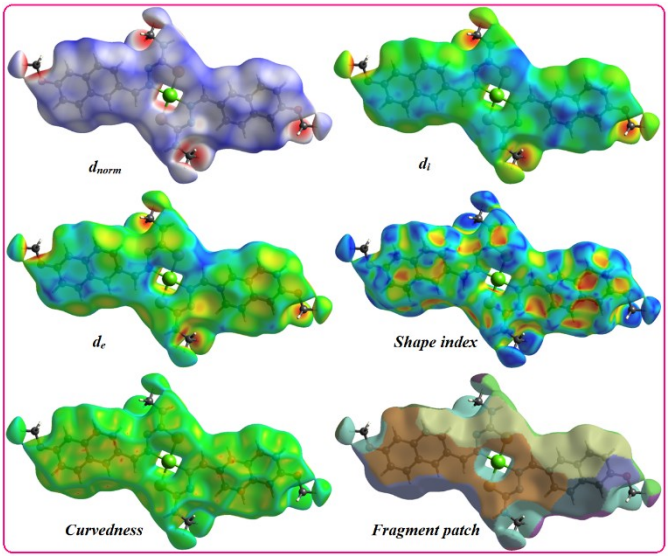

Figure S36. Graphical view of the Hirshfeld surfaces (HS) of the bis-Schiff base nickel(II) complex [Ni(L)$_2$](**2**).; red spots represents the closest contacts and blue colour the most distant contacts.

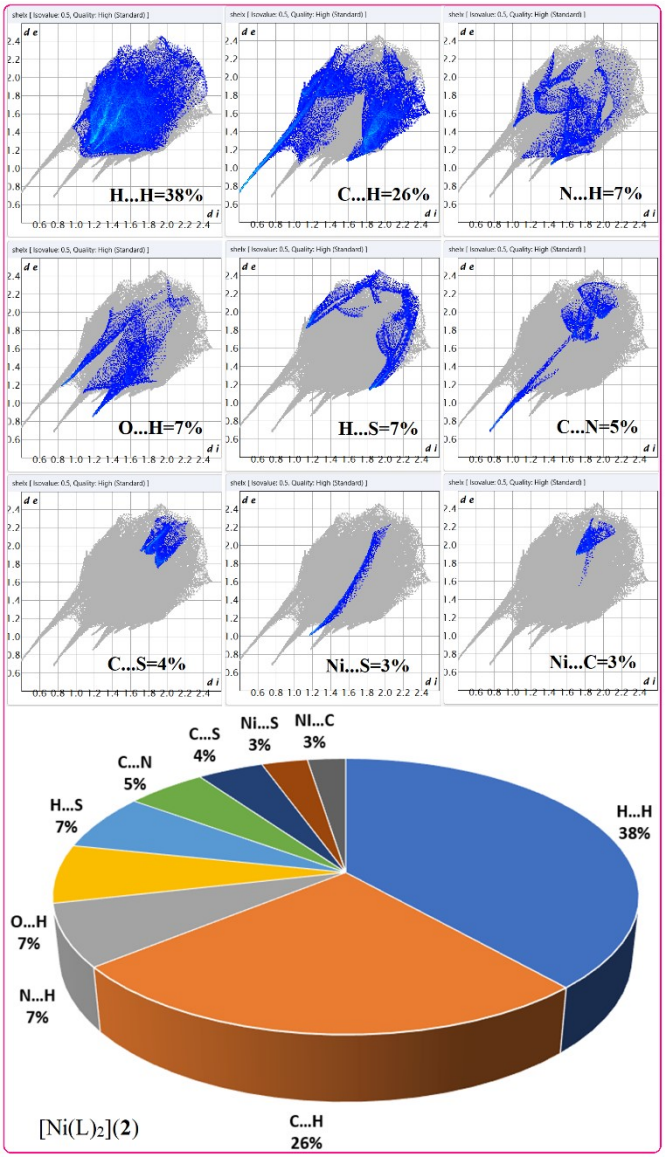

Figure S37. Fingerprint plot for nickel(II) complex [Ni(L)$_2$](**2**) showing the percentage of contact that contributed to the total Hirshfeld surface (HS) area of the molecules and its pie chart; d_i, and d_e are the distances from the surface to the nearest atoms interior and exterior to the surface, respectively.

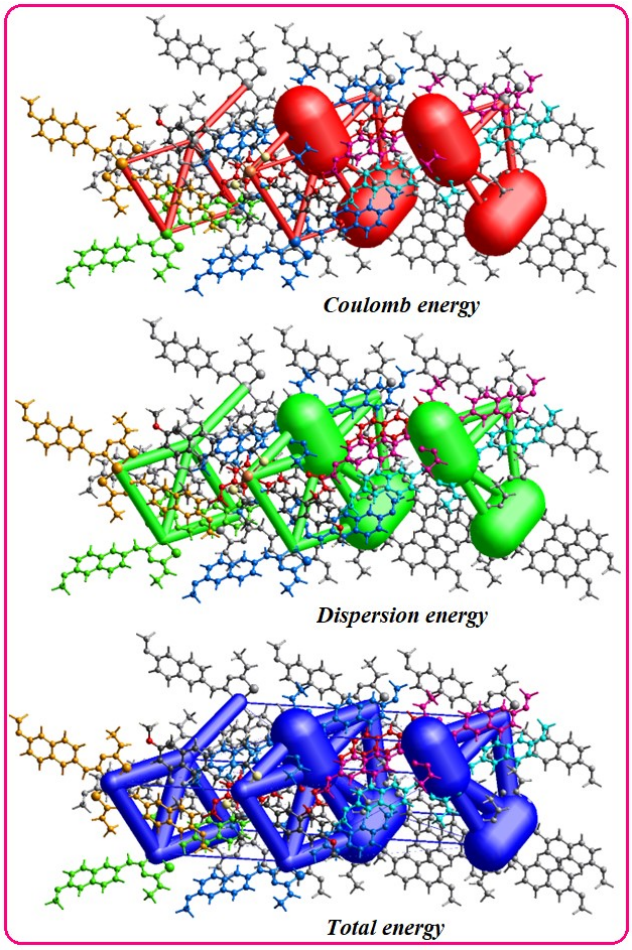

Figure S38. 3D-Graphical view of interaction energy framework diagram of the bis-Schiff base copper (II) complex $[Cu(L)_2]$(**1**) computed at B3LYP/6-31G(*d, p*)/DFT. Hydrogen atoms is omitted for clarity and all diagrams used the same cylindrical scale of 300 for energies.

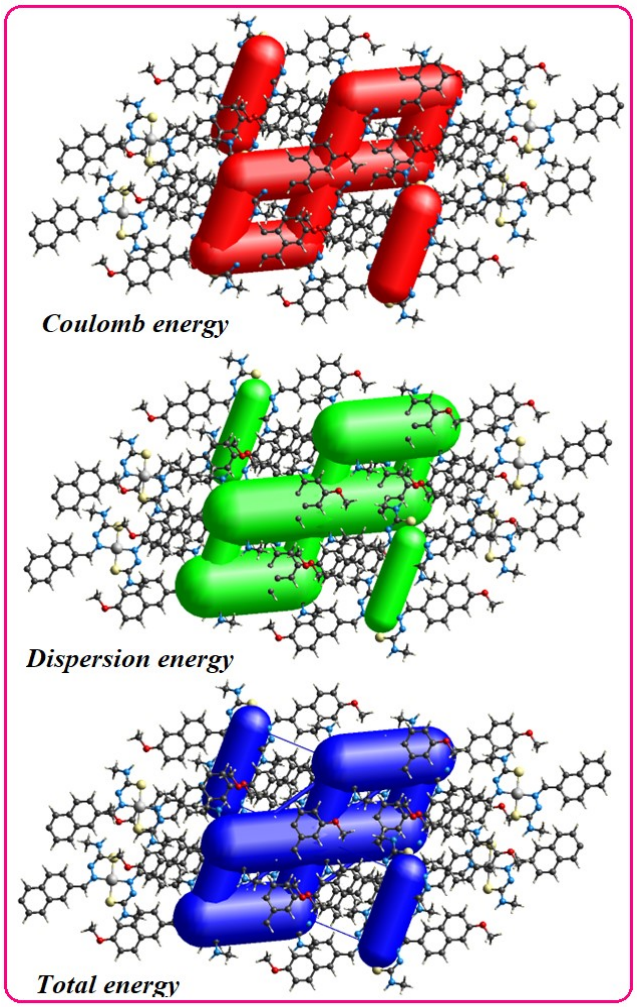

Figure S39. 3D-Graphical view of interaction energy framework diagram of the bis-Schiff base nickel(II) complex $[Ni(L)_2]$(**2**) computed at B3LYP/6-31G(*d, p*)/DFT. Hydrogen atoms is omitted for clarity and all diagrams used the same cylindrical scale of 300 for energies.

Interaction Energies (kJ/mol) [$Cu(L)_2$](**1**)
R is the distance between molecular centroids (mean atomic position) in Å.

Total energies, only reported for two benchmarked energy models, are the sum of the four energy components, scaled appropriately (see the scale factor table below)

	N	Symop	R	Electron Density	E_ele	E_pol	E_dis	E_rep	E_tot
	1	x+1/2, -y+1/2, z+1/2	9.99	B3LYP/6-31G(d,p)	-3.7	-1.6	-49.9	16.3	-38.6
	1	x, y, z	13.62	B3LYP/6-31G(d,p)	0.0	-4.1	0.0	0.0	-3.0
	0	-x, -y, -z	4.01	B3LYP/6-31G(d,p)	-50.6	-8.9	-212.2	251.1	-89.7
	1	-x+1/2, y+1/2, -z+1/2	12.69	B3LYP/6-31G(d,p)	0.0	-0.2	0.0	0.0	-0.1
	0	-x, -y, -z	18.35	B3LYP/6-31G(d,p)	0.0	-1.1	0.0	0.0	-0.8
	1	x+1/2, -y+1/2, z+1/2	21.06	B3LYP/6-31G(d,p)	0.0	-0.4	0.0	0.0	-0.3
	2	-x+1/2, y+1/2, -z+1/2	9.41	B3LYP/6-31G(d,p)	-6.5	-1.1	-46.7	28.5	-30.7
	0	-x, -y, -z	12.51	B3LYP/6-31G(d,p)	0.0	-1.7	0.0	0.0	-1.2
	0	-x, -y, -z	10.30	B3LYP/6-31G(d,p)	-7.1	-2.0	-39.4	11.4	-36.2
	1	-x+1/2, y+1/2, -z+1/2	19.67	B3LYP/6-31G(d,p)	0.0	-0.2	0.0	0.0	-0.2

Scale factors for benchmarked energy models
See Mackenzie et al. IUCrJ (2017)

Energy Model	k_ele	k_pol	k_disp	k_rep
CE-HF ... HF/3-21G electron densities	1.019	0.651	0.901	0.811
CE-B3LYP ... B3LYP/6-31G(d,p) electron densities	1.057	0.740	0.871	0.618

Interaction Energies (kJ/mol) [$Ni(L)_2$](**2**)
R is the distance between molecular centroids (mean atomic position) in Å.

Total energies, only reported for two benchmarked energy models, are the sum of the four energy components, scaled appropriately (see the scale factor table below)

	N	Symop	R	Electron Density	E_ele	E_pol	E_dis	E_rep	E_tot
	1	x, y, z	13.43	B3LYP/6-31G(d,p)	0.0	-12.2	0.0	0.0	-9.0
	1	x, y, z	7.92	B3LYP/6-31G(d,p)	-30.5	-8.1	-77.6	46.6	-77.1
	0	x, y, z	14.20	B3LYP/6-31G(d,p)	0.0	-0.2	0.0	0.0	-0.2
	1	x, y, z	8.27	B3LYP/6-31G(d,p)	-32.7	-14.2	-145.5	90.2	-116.0
	0	x, y, z	12.84	B3LYP/6-31G(d,p)	0.0	-2.7	0.0	0.0	-2.0

Scale factors for benchmarked energy models
See Mackenzie et al. IUCrJ (2017)

Energy Model	k_ele	k_pol	k_disp	k_rep
CE-HF ... HF/3-21G electron densities	1.019	0.651	0.901	0.811
CE-B3LYP ... B3LYP/6-31G(d,p) electron densities	1.057	0.740	0.871	0.618

Figure S40. Energy framework CE-B3LYP estimates of energy components and total energies (kJ/mol) for the closest intermolecular interactions in the copper(II) complex [$Cu(L)_2$](**1**) and nickel(II) complex [$Ni(L)_2$](**2**).

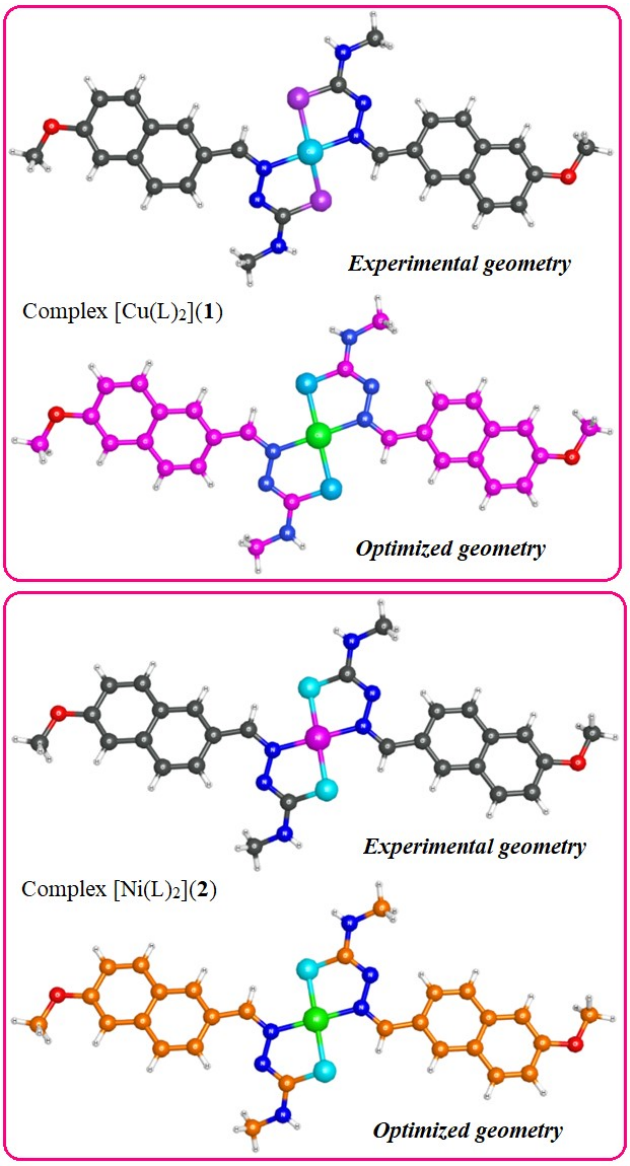

Figure S41. Experimental and optimized geometry of the newly synthesized copper(II) complex [$Cu(L)_2$](**1**) and nickel(II) complex [$Ni(L)_2$](**2**).

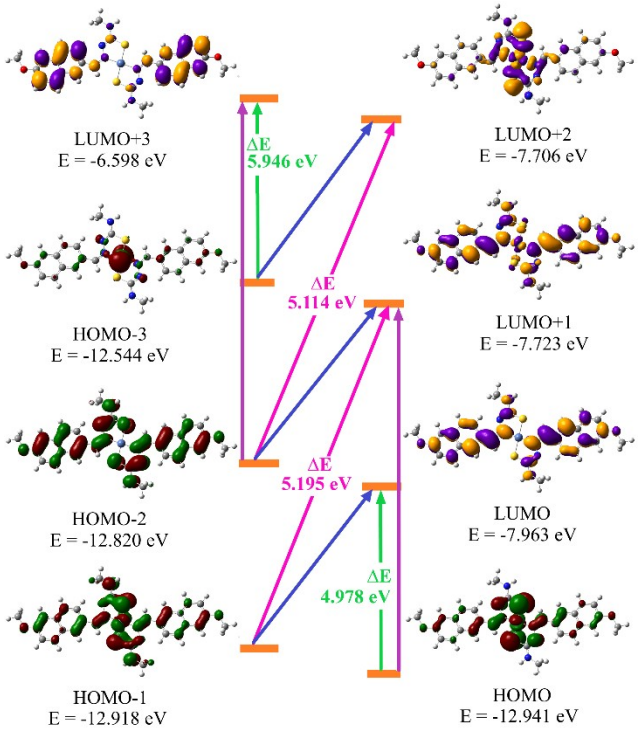

Figure S42. DFT calculated HOMO-LUMO molecular orbital energy level diagram of the bis-Schiff base nickel(II) complex $[Ni(L)_2]$(**2**).

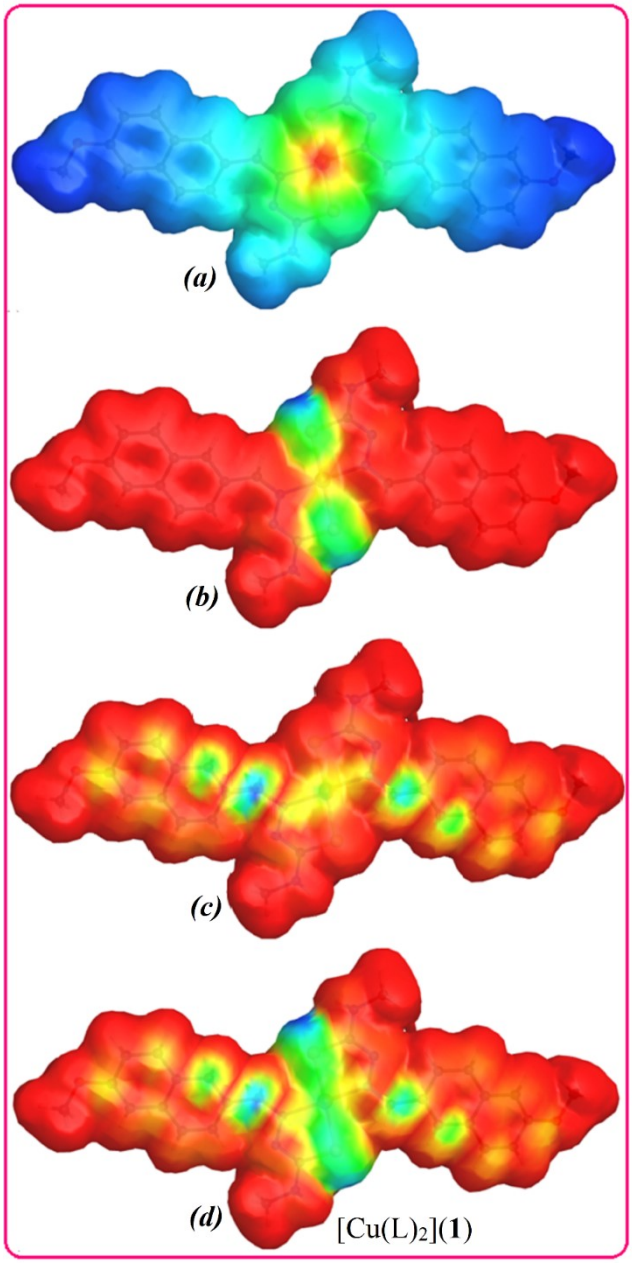

Figure S43. The molecular electrostatic potential (MEPs) surfaces of the bis-Schiff base copper (II) complex $[Cu(L)_2]$(**1**); (a) Electron potential (b) Electrophilic frontier density (c) Nucleophilic frontier density (d) Radicial frontier density.

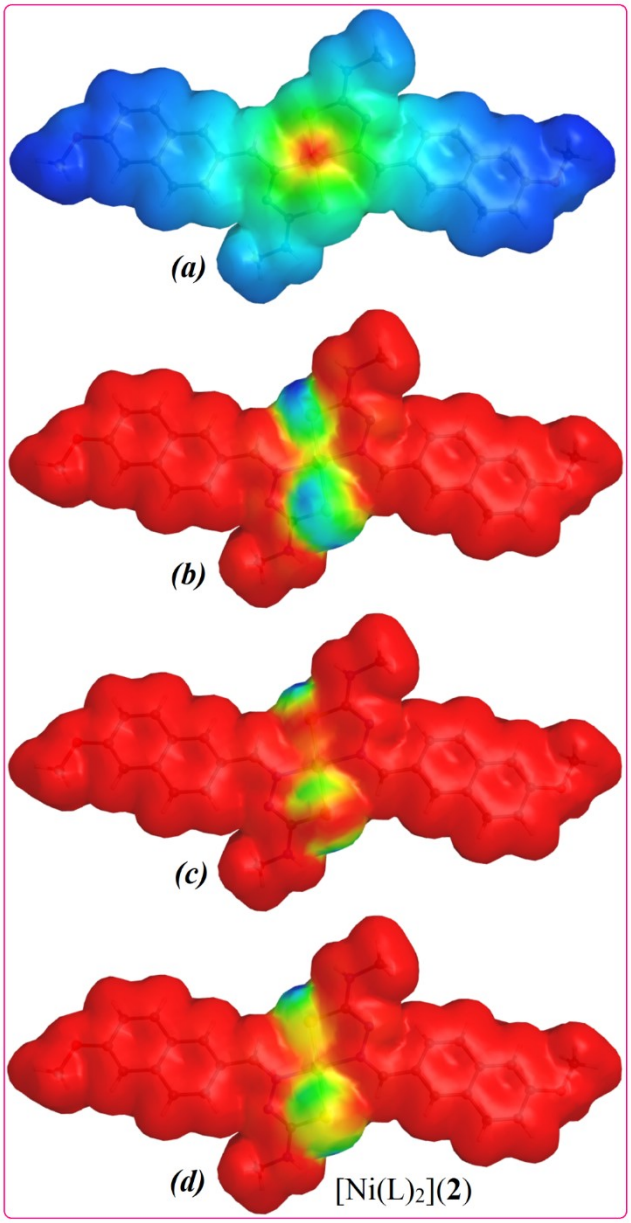

Figure S44. The molecular electrostatic potential (MEPs) surfaces of the bis-Schiff base nickel(II) complex $[Ni(L)_2]$(**1**); (a) Electron potential (b) Electrophilic frontier density (c) Nucleophilic frontier density (d) Radicial frontier density.

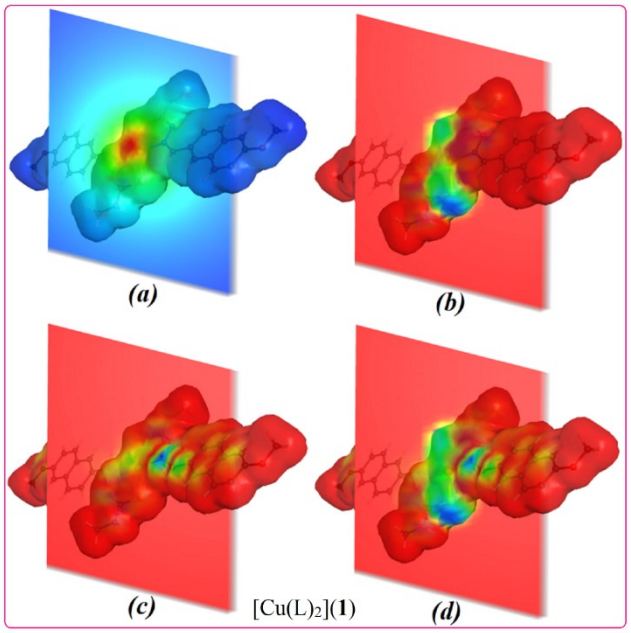

Figure S45. Slice view of the molecular electrostatic potential (MEPs) surfaces of the bis-Schiff base copper(II) complex $[Cu(L)_2]$(**1**); (a) Electron potential (b) Electrophilic frontier density (c) Nucleophilic frontier density (d) Radicial frontier density.

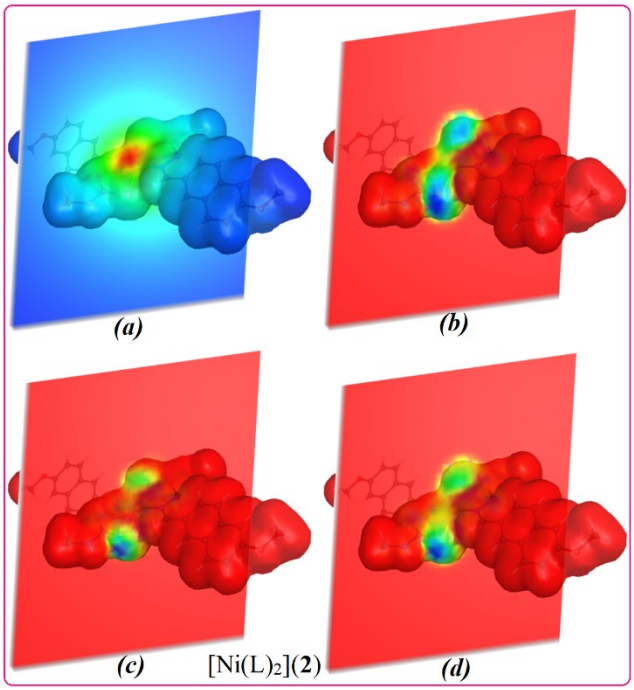

Figure S46. Slice view of the molecular electrostatic potential (MEPs) surfaces of the bis-Schiff base nickel(II) complex $[Ni(L)_2]$(**2**); (a) Electron potential (b) Electrophilic frontier density (c) Nucleophilic frontier density (d) Radicial frontier density.

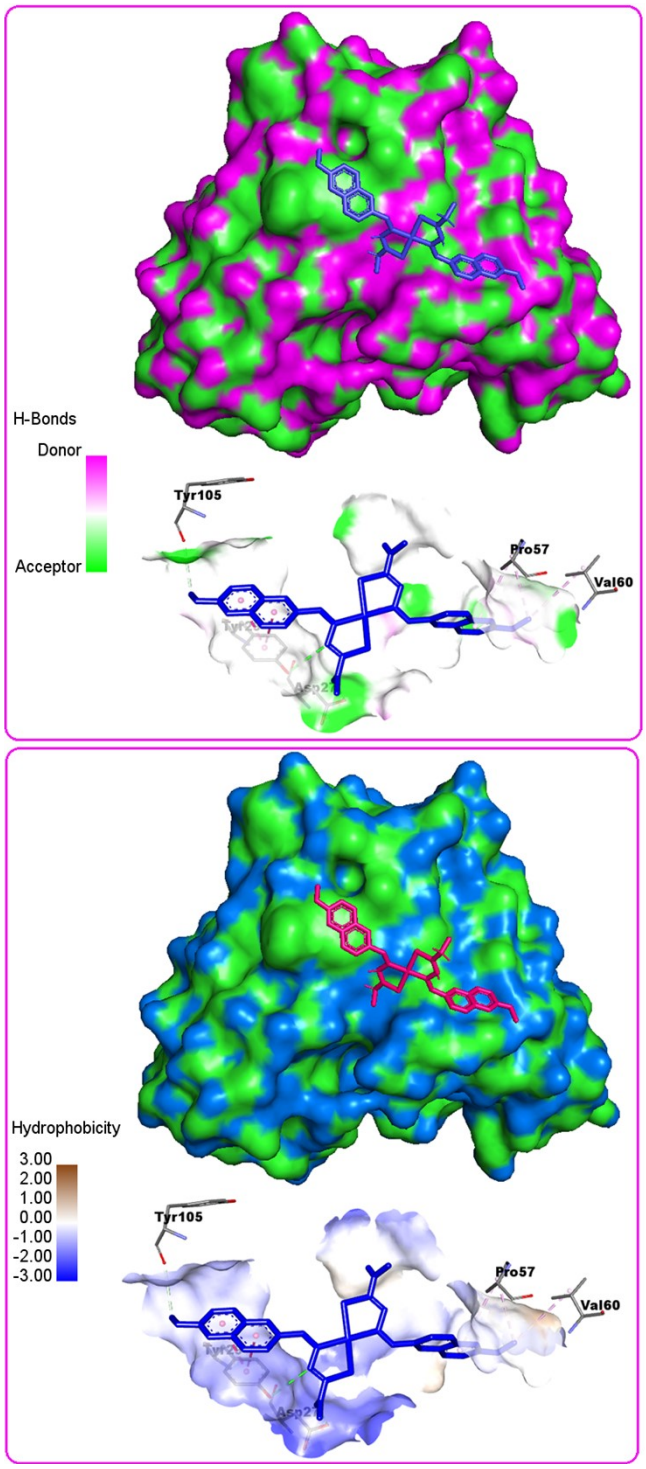

Figure S47. Graphical view of total density surfaces with H-bond (top figure) and Hydrophobicity (bottom figure) of the docked copper(II) complex $[Cu(L)_2]$(**1**) with interacting residues inside the active site of the SARS-CoV-2 RBD protein(PDB ID: 6WKP).

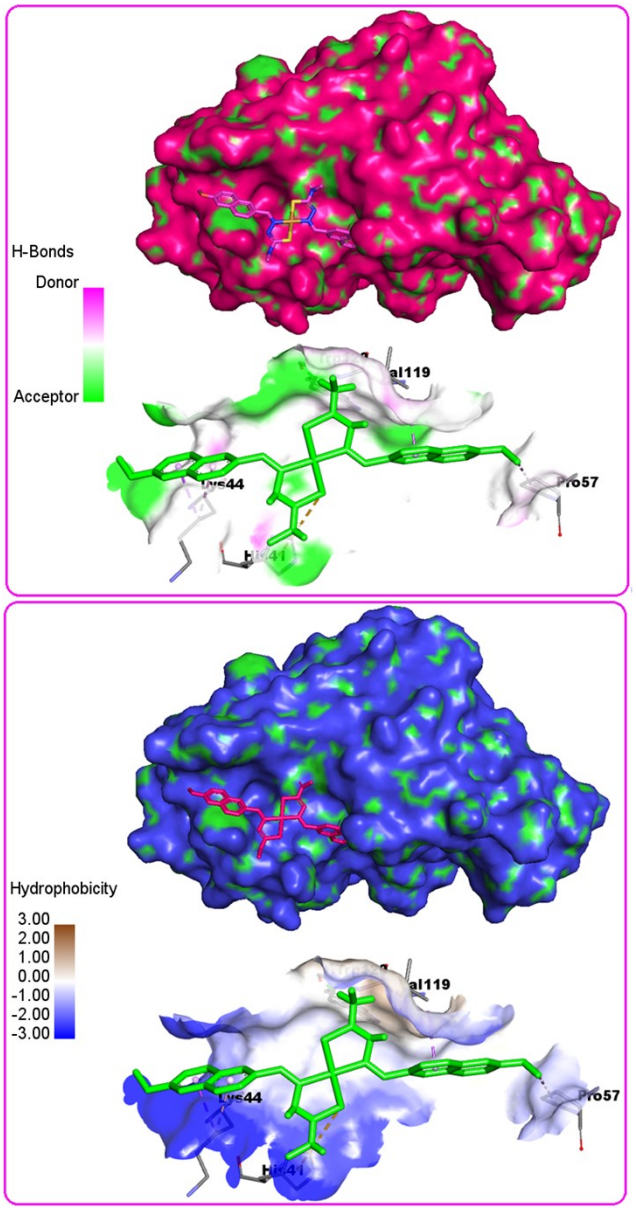

Figure S48. Graphical view of total density surfaces with H-bond (top figure) and Hydrophobicity (bottom figure) of the docked nickel(II) complex $[Ni(L)_2]$(**2**) with interacting residues inside the active site of the SARS-CoV-2 RBD protein(PDB ID: 6WKP).

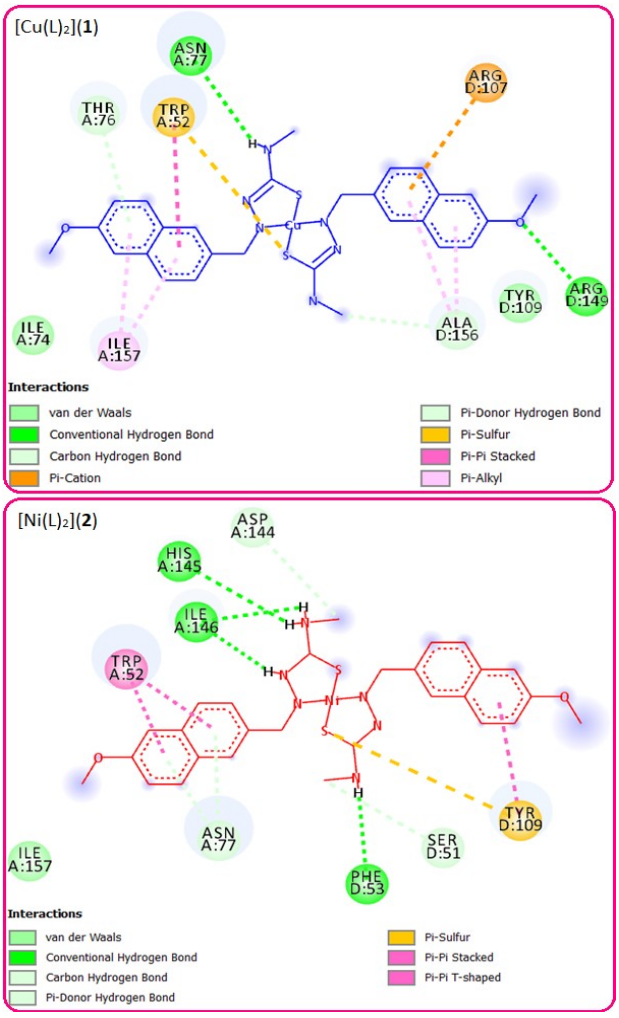

Figure S49. 2D representation of the docked copper(II) complex $[Cu(L)_2]$(**1**) and nickel(II) complex $[Ni(L)_2]$(**2**) with interacting residues inside the active site of the SARS-CoV-2 RNA binding protein(PDB ID: 6WKP).

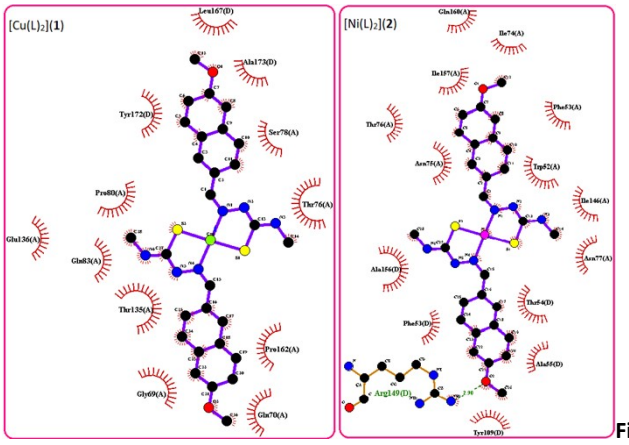

Figure S50. 3D view of the docked copper(II) complex $[Cu(L)_2]$(**1**) and nickel(II) complex $[Ni(L)_2]$(**2**) with interacting residues inside the active site of the SARS-CoV-2 RNA binding protein (PDB ID: 6WKP).

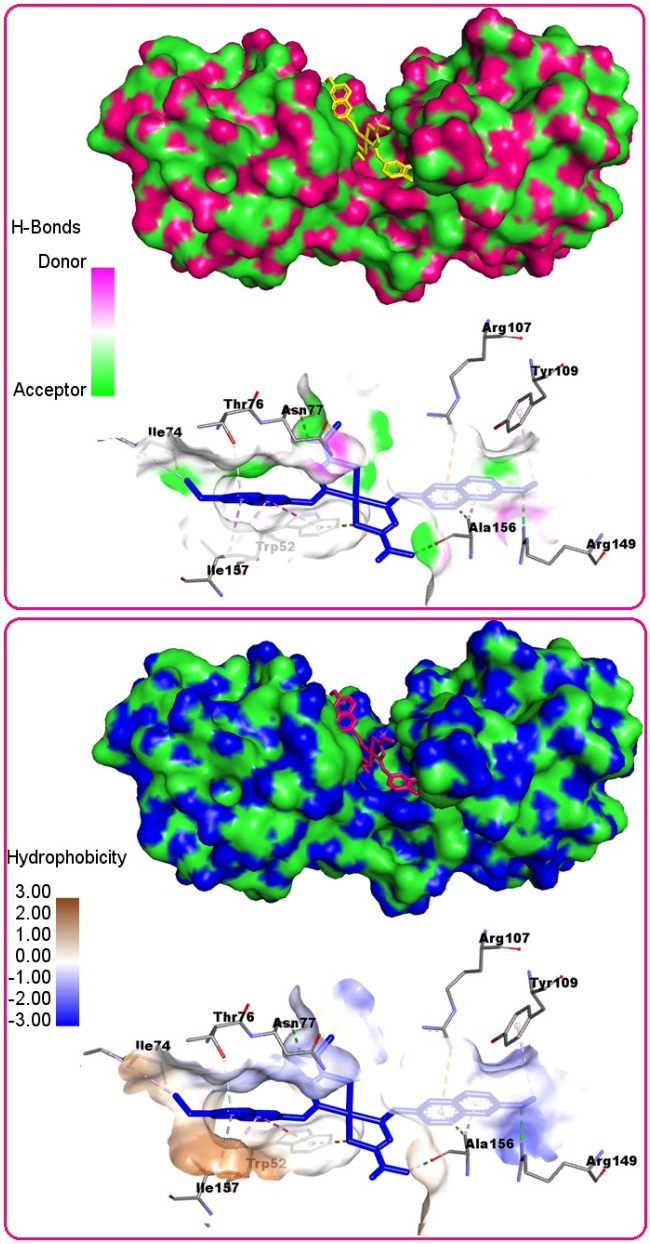

Figure S51. Graphical view of total density surfaces with H-bond (top figure) and Hydrophobicity (bottom figure) of the docked copper(II) complex $[Cu(L)_2]$(**1**) with interacting residues inside the active site of the Omicron protein (PDB ID: 7WRL).

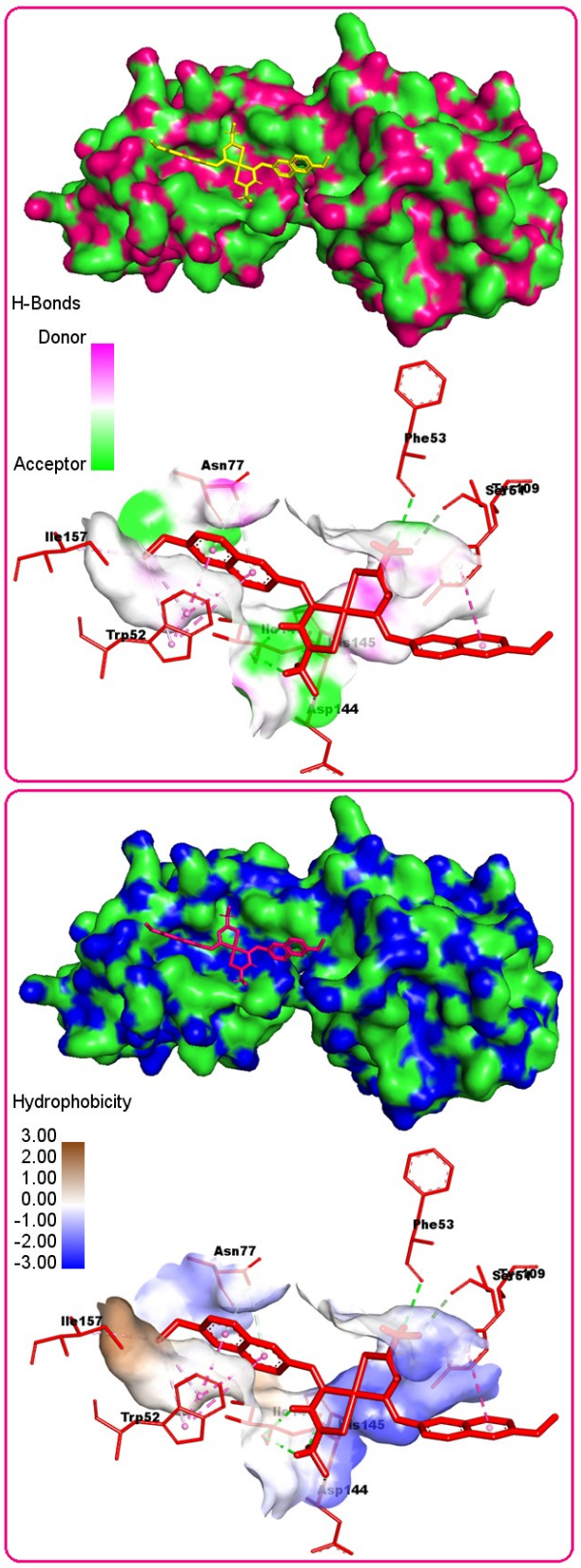

Figure S52. Graphical view of total density surfaces with H-bond (top figure) and Hydrophobicity (bottom figure) of the docked nickel(II) complex $[Ni(L)_2]$(**2**) with interacting residues inside the active site of the Omicron protein (PDB ID: 7WRL).

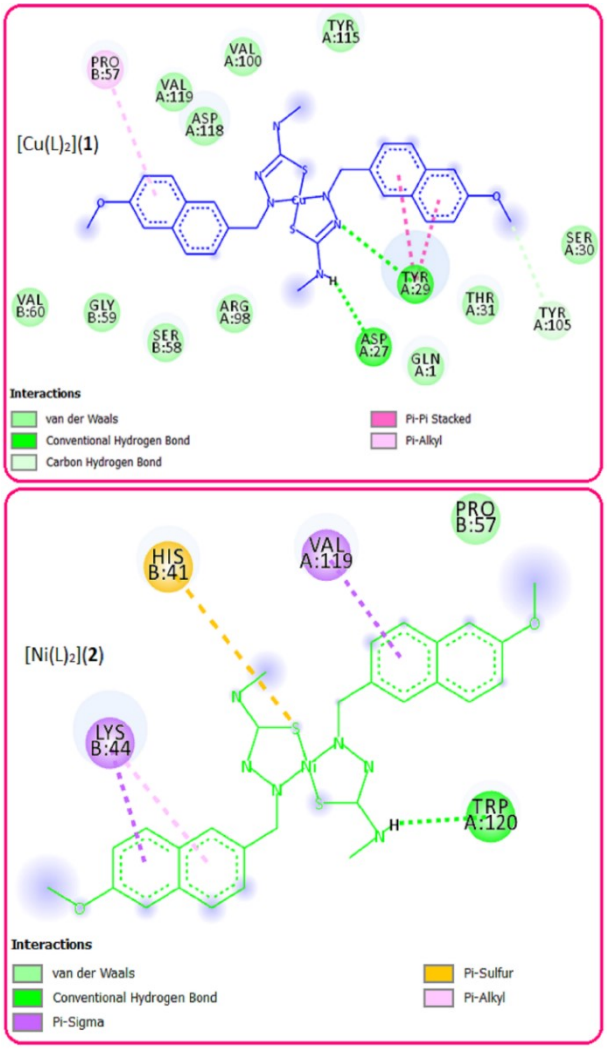

Figure S53. 2D representation of the docked copper(II) complex $[Cu(L)_2]$ (**1**) and nickel(II) $[Ni(L)_2]$(**2**)with interacting residues inside the active site of the Omicron RBD protein(PDB ID: 7WRL).

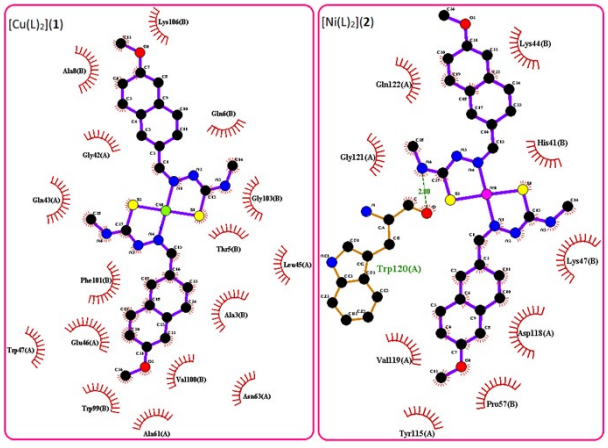

Figure S54. 3D view of the docked copper(II) complex $[Cu(L)_2]$(**1**) and nickel(II) complex $[Ni(L)_2]$(**2**) with interacting residues inside the active site of the Omicron RBD protein (PDB ID: 7WRL).

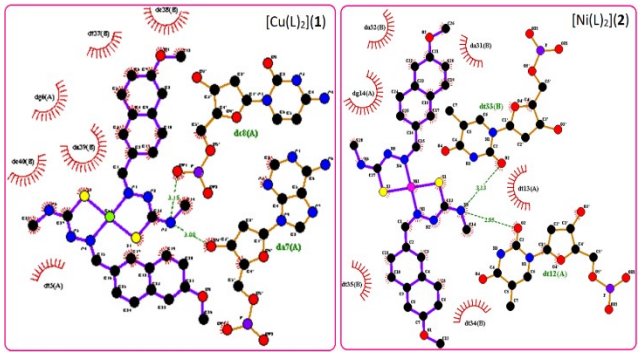

Figure S55. 3D view of the docked copper(II) complex $[Cu(L)_2]$(**1**) and nickel(II) complex $[Ni(L)_2]$(**2**) with interacting residues inside the active site of the DNA binding protein (PDB ID: 7UV6).

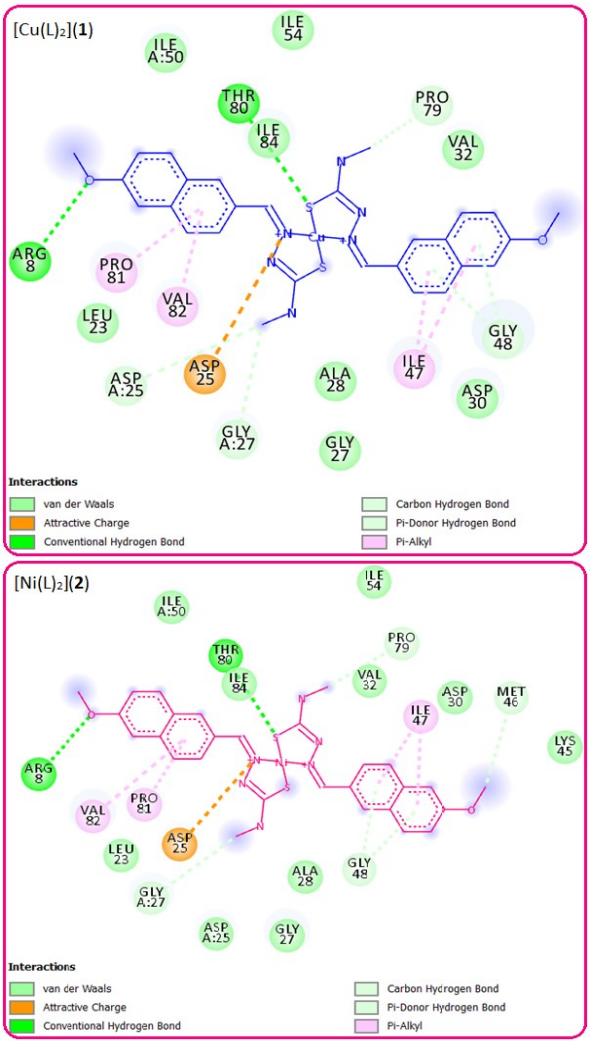

Figure S56. 2D representation of the docked copper(II) complex $[Cu(L)_2]$(**1**) and nickel(II) complex $[Ni(L)_2]$(**2**) with interacting residues inside the active site of the HIV-1 protease (PDB ID: 8CI7).

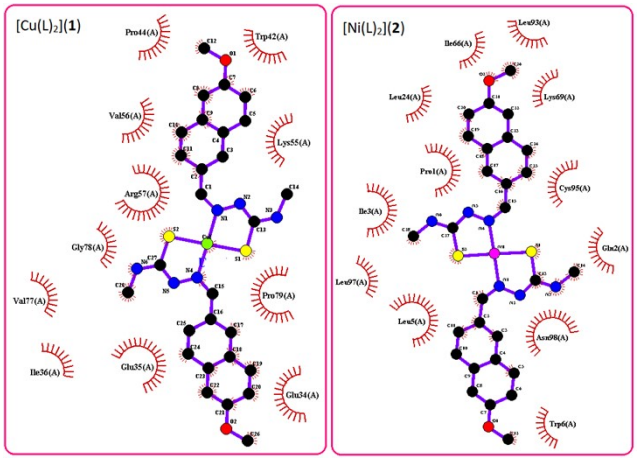

Figure S57. 3D view of the docked copper(II) complex $[Cu(L)_2]$(**1**) and nickel(II) complex $[Ni(L)_2]$(**2**) with interacting residues inside the active site of the HIV-1 protease (PDB ID: 8CI7).

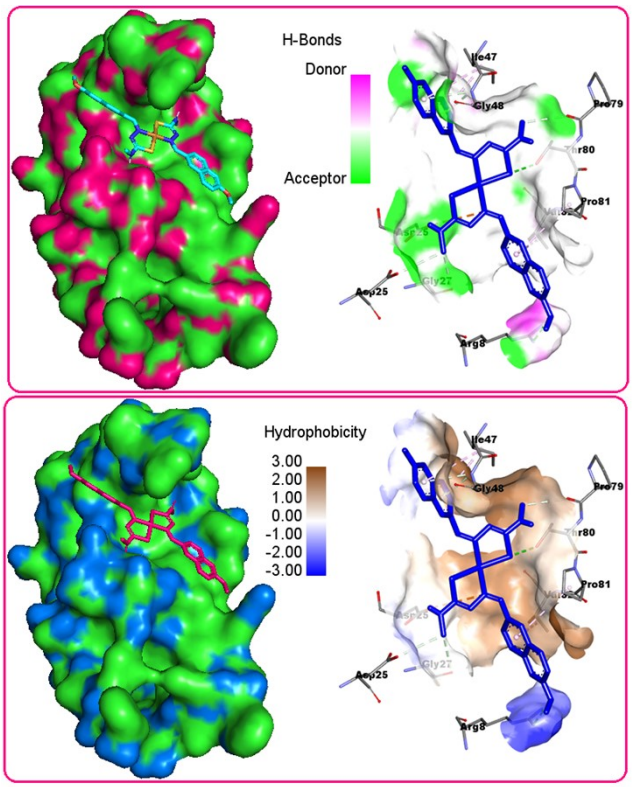

Figure S58. Graphical view of total density surfaces with H-bond (top figure) and Hydrophobicity (bottom figure) of the docked copper(II) complex $[Cu(L)_2]$(**1**) with interacting residues inside the active site of the HIV-1 protease (PDB ID: 8CI7).

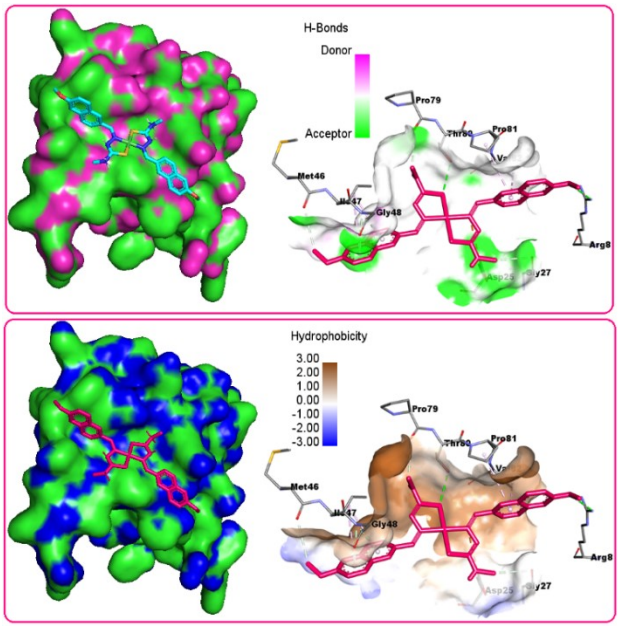

Figure S59. Graphical view of total density surfaces with H-bond (top figure) and Hydrophobicity (bottom figure) of the docked nickel(II) complex $[Ni(L)_2]$(**2**) with interacting residues inside the active site of the HIV-1 protease (PDB ID: 8CI7).

Table S1. Thermal degradation of the copper(II) complex $[Cu(L)_2]$(**1**) and nickel(II) complex $[Ni(L)_2]$(**2**).

Compounds	DSC range (ºC)	Process	ΔH (J/g)	TG-DTG peak(ºC)	Mass loss (%)	Assignments
$[Cu(L)_2]$(**1**)	124.8	Exo	40.86	123.1 227.8 342.0	-52.09 -06.55 -18.68	Cleavage of CH=N- Residue Leaving CuO
$[Ni(L)_2]$(**2**)	268	Exo	176.9	272.5 343.5	-16.62 -33.35	Residue Leaving NiO

Table S2. A correlation between binding parameters of CT-DNA and BSA with tested complexes $[Cu(L)_2]$(1) and $[Ni(L)_2]$(2) at pH of 7.4 by UV-Vis and fluorescence spectral titration.

Compound		k_b (M^{-1})	k_a (M^{-1})	k_q (M^{-1})	n
$[Cu(L)_2]$(**1**)	DNA	3.72×10^4	4.98×10^4	6.41×10^{12}	1.06
	BSA	4.32×10^3	3.87×10^4	5.95×10^{12}	0.98
$[Ni(L)_2]$(**2**)	DNA	4.43×10^4	4.11×10^4	6.15×10^{12}	1.01
	BSA	5.14×10^3	3.35×10^4	5.23×10^{12}	0.93

Table S3. Crystallographic data and structure refinement parameters of the copper(II) complex $[Cu(L)_2]$(**1**) and nickel(II) $[Ni(L)_2]$(**2**).

Crystallographic data	$[Cu(L)_2]$(**1**)	$[Ni(L)_2]$(**2**)
Empirical Formula	$C_{28}H_{28}CuN_6O_2S_2$	$C_{28}H_{28}N_6NiO_2S_2$
Mw ($gmol^{-1}$)	608.22	603.39
temp (K)	120(2)	100(2)
λ (Mo Kα), (Å)	0.71073	0.71073
crystal system	Monoclinic	Triclinic
space group	$P2_1/n$	P_{-1}
a (Å)	13.619(3)	7.9246(5)
b (Å)	13.029(3)	8.2663(4)
c (Å)	14.861(4)	10.8997(7)
α (°)	90	82.906(2)
β (°)	97.778(8)	82.315(2)
γ (°)	90	67.927(2)
V (Å^3)	2612.7(11)	653.64(7)
Z	4	1
D_{calc} (mg/m^3)	1.546	1.533
μ (mm^{-1})	1.036	0.942
F(000)	1260	314
Crystal size(mm^3)	0.215 × 0.086 × 0.042	0.316 × 0.195 × 0.178
Theta range for data collection(°)	2.464 to 25.299	3.350 to 28.320
Limiting indices	-16<=h<=16, -15<=k<=15, -17<=l<=17	-10<=h<=10, -11<=k<=11, -14<=l<=14
Reflections collected/ unique	31863/4711 [R(int) = 0.2233]	26284 / 3235 [R(int) = 0.0458]
Completeness to = 25.242	99.4 %	99.6 %
Absorption Correction	Semi-empirical from equivalents	Semi-empirical from equivalents
Max. And min. transmission	0.7452 and 0.4145	0.7457 and 0.5916
Refinement method	Full-matrix -least squares on F^2	Full-matrix least-squares on F^2
Data/restrains/parameters	4711/2/362	3235 / 0 / 183
Goodness-of-fit (GOF) on F^2	1.049	1.056
R_1 [$I > 2\sigma(I)$][a]	R1 = 0.0721, wR2 = 0.1452	R1 = 0.0282, wR2 = 0.0760
wR_2 (all data)[b]	R1 = 0.1318, wR2 = 0.1683	R1 = 0.0299, wR2 = 0.0780
Largest diff. Peak and hole(A^{-3})	0.553 and -0.773	0.453 and -0.293
CCDC Number	2350278	2350279

[a] $R_1 = \sum||F_o| - |F_c|| / \sum|F_o|$; [b] $wR_2 = \{\sum [w(F_o^2 - F_c^2)^2] / \sum [w(F_o^2)^2]\}^{1/2}$

Table S4. Selected bond distances (Å) and bond angles (°) found

in the copper(II) complex $[Cu(L)_2]$(**1**) and nickel(II) complex $[Ni(L)_2]$(**2**).

Complex $[Cu(L)_2]$(**1**)			
Bond lengths (Å)			
Cu(1)-N(1)	2.023(5)	Cu(1)-S(2)	2.2593(18)
Cu(1)-N(4)	2.028(5)	Cu(1)-S(1)	2.2765(17)
Bond angles (°)			
N(1)-Cu(1)-N(4)	177.6(2)	N(1)-Cu(1)-S(1)	83.89(15)
N(1)-Cu(1)-S(2)	95.05(15)	N(4)-Cu(1)-S(1)	96.51(14)
N(4)-Cu(1)-S(2)	84.06(15)	S(2)-Cu(1)-S(1)	168.12(7)
Complex $[Ni(L)_2]$(**2**)			
Bond lengths (Å)			
Ni(1)-N(1)	1.923(11)	Ni(1)-S(1)	2.186(3)
N(1)-N(2)	1.3976(16)	C(1)-N(1)	1.3017(17)
Bond angles (°)			
N(1)-Ni(1)-N(1)#1	180.0	N(1)-Ni(1)-S(1)	85.51(4)
N(1)#1-Ni(1)-S(1)	94.49(4)	N(1)-Ni(1)-S(1)#1	94.49(4)
N(1)#1-Ni(1)-S(1)#1	85.51(4)	S(1)-Ni(1)-S(1)#1	180.0(15)

Table S5. Hydrogen bond parameters found in the copper(II) complex $[Cu(L)_2]$(**1**) and nickel(II) complex $[Ni(L)_2]$(**2**).

D-H...A	D-H (Å)	H-A (Å)	D-A (Å)	D-H-A (°)
Complex $[Cu(L)_2]$(**1**)				
C(1)-H(1)...S(2)	0.95	2.48	3.176(7)	129.7
C(6)-H(6)...S(1)#1	0.95	2.96	3.840(6)	155.4
C(12)-H(12C)...O(2)#2	0.98	2.59	3.471(8)	150.2
C(15)-H(15)...S(1)	0.95	2.50	3.203(6)	131.2
C(20)-H(20)...S(2)#3	0.95	2.94	3.888(6)	173.2
N(3)-H(3N)...O(1)#3	0.86(2)	2.34(3)	3.191(6)	167(6)
N(6)-H(6N)...O(2)#1	0.87(2)	2.50(5)	3.134(6)	130(5)
Complex $[Ni(L)_2]$(**2**)				
C(1)-H(1)...S(1)#1	0.95	2.46	3.089(14)	123.8
C(12)-H(12C)...N(2)#2	0.98	2.56	3.491(2)	157.8
N(3)-H(3A)...O(1)#3	0.77(2)	2.27(2)	3.011(16)	162(2)

Symmetry transformations used to generate equivalent atoms:

#1 x-1/2,-y+3/2,z-1/2 #2 -x+1,-y+1,-z+1 #3 x-1,y,z #4 -x,-y+1,-z+1 for $[Zn(L)(en)]ClO_4$(**1**); and #1-x+1/2, y+1/2, -z+1/2#2-x+1/2, y-1/2, -z+1/2 for $[Zn(L)_2]$ (**2**).

0 atoms	0.00%	have non-positive definite ADPs
0 atoms	0.0%	have anisotropy < 0.10
0 atoms	0.0%	have anisotropy < 0.20
0 atoms	0.0%	in the protein are perfectly isotropic
	1	pairs of neighboring atoms have S(u,v) < 0.975
	0	C-N linkages have correlation < 0.95

	Anisotropy		# atoms
	Mean	Sigma	
Protein			**0**
Solvent			**0**
Hetatms	**0.451**	**0.138**	**39**
Total	**0.451**	**0.138**	**39**
CU	**0.508**	**0.000**	**1**
S	**0.410**	**0.011**	**2**
O	**0.395**	**0.071**	**2**
N	**0.565**	**0.171**	**6**
C	**0.431**	**0.132**	**28**

$[Cu(L)_2]$(**1**)

0 atoms	0.00%	have non-positive definite ADPs
0 atoms	0.0%	have anisotropy < 0.10
0 atoms	0.0%	have anisotropy < 0.20
0 atoms	0.0%	in the protein are perfectly isotropic
	0	pairs of neighboring atoms have S(u,v) < 0.975
	0	C-N linkages have correlation < 0.95

	Anisotropy		# atoms
	Mean	Sigma	
Protein			**0**
Solvent			**0**
Hetatms	**0.635**	**0.147**	**39**
Total	**0.635**	**0.147**	**39**
C	**0.666**	**0.135**	**28**
N	**0.623**	**0.154**	**6**
O	**0.390**	**0.000**	**2**
S	**0.471**	**0.000**	**2**
NI	**0.655**	**0.000**	**1**

$[Ni(L)_2]$(**2**)

Table S6. Summary of anisotropic displacement parameters (ADPs, $Å^2$ x 10^3) results for copper(II) complex $[Cu(L)_2]$ (**1**) and nickel(II) complex $[Ni(L)_2]$(**2**).

Table S7. Quantum chemical parameters or global reactivity descriptors (units in eV) as well as FMO energy gap values of the bis-Schiff base metal(II) complexes $[Cu(L)_2]$(**1**) and $[Ni(L)_2]$(**2**).

Molecular descriptors and energy gap (ΔE_g)	$[Cu(L)_2]$(**1**)	$[Ni(L)_2]$(**2**)
E_{LUMO}	-7.953	-7.963
E_{HOMO}	-12.254	-12.941
ΔE_g	4.301	4.978
$E_{LUMO\ (+1)}$	-7.937	-7.723
$E_{HOMO\ (-1)}$	-12.067	-12.918
ΔE_g	4.130	5.195
$E_{LUMO\ (+2)}$	-7.676	-7.706
$E_{HOMO\ (-2)}$	-12.018	-12.820
ΔE_g	4.342	5.114
$E_{LUMO\ (+3)}$	-7.666	-6.598
$E_{HOMO\ (-3)}$	-12.001	-12.544
ΔE_g	4.335	5.946
Ionization potential, IP = - E_{HOMO}	12.254	12.941
electron affinity, EA = -E_{LUMO}	7.953	7.963
electro negativity, χ = (IP + EA)/2	10.103	10.452
chemical potential, μ = -(IP + EA)/2	-10.103	-10.452
global softness, $\sigma = 1/2\eta$	0.23	0.20
global hardness, η = (IP - EA)/2	2.15	2.49
Electrophilicity index, $\omega = \mu^2 / 2\eta$	23.74	21.94

Energy gap (ΔE) = E_{LUMO}-$E_{HOMO;}$ units in eV

Table S8. Established structure activity relationship (SAR) between the experimental geometries of the bis-Schiff base metal(II) complexes $[Cu(L)_2]$(**1**) and $[Ni(L)_2]$(**2**) determined by the single crystal X-ray diffraction technique and the theoretical geometries observed upon interactions against SARS-CoV-2 RNA binding protein (PDB ID: 6WKP) and Omicron RBD protein (PDB ID: 7WRL).

Complexes	Experimental bond lengths (Å)		Docked complexes inside SARS-CoV-2 RBD protein and Omicron RBD protein with bond lengths (Å)			
			PDB ID: 6WKP		PDB ID: 7WRL	
$[Cu(L)_2]$(**1**)	Cu(1)-N(1)	2.023(5)	Cu(1)-N(1)	2.02128	Cu(1)-N(1)	2.02191
	Cu(1)-N(4)	2.028(5)	Cu(1)-N(4)	2.02847	Cu(1)-N(4)	2.02785
	Cu(1)-S(2)	2.2593(18)	Cu(1)-S(2)	2.25938	Cu(1)-S(2)	2.26031
	Cu(1)-S(1)	2.2765(17)	Cu(1)-S(1)	2.27586	Cu(1)-S(1)	2.27555
$[Ni(L)_2]$(**2**)	Ni(1)-N(1)	1.923(11)	Ni(1)-N(1)	1.92364	Ni(1)-N(1)	1.92332
	Ni(1)-S(1)	2.186(3)	Ni(1)-S(1)	2.1863	Ni(1)-S(1)	2.18594
	N(1)-N(2)	1.3976(16)	N(1)-N(2)	1.39799	N(1)-N(2)	1.39795
	C(1)-N(1)	1.3017(17)	C(1)-N(1)	1.3009	C(1)-N(1)	1.30057

Table S9. Comparison of binding energies (ΔG) and inhibition / dissociation constants (K_i/K_d) of some metal complexes against SARS-CoV-2 (Omicron) virus target proteins obtained from in-silico docking study.

Sl. No.	Complexes	binding energies (kcal/mol)	inhibition / dissociation constants, [Ki(μM)	Ref.
1	$[Ni(L)]_2$	-11.2	7.134	22
2	$[Ni(L)]_n$	-10.5	6.213	22
3	$[Zn(L)(en)]ClO_4$	-9.1	2.938	23
4	$[Zn(L)_2]$ (**2**)	-10.2	1.296	23
5	$[Ni_3(\mu\text{-}L)_2(bipy)_3]$	-8.9	2.373	24
6	$[Ni(L^1)](PPh_3)]DMF$	-8.93	0.28461	25
7	$[Ni(L^2)]$	-5.7	65.87	25
8	$[Cu(L^1)_2]$	-9.8	2.912	26
9	$[Cu(L^2)_2]$	-9.4	2.813	26
10	$[Cu(L^1)_2]$	-8.7	2.585	27
11	$[Cu(L^2)(CH_3OH)(Cl)]$	-8.2	2.395	27
12	$[Ni(L)_2]$	-7.2	-	57
13	$[Cu(L)_2]$	-9.7	-	57
14	[Cu(L)(Phen)]	-6.18	0.76	76(a)
15	$[Ni(L^1)(Phen)_2]ClO_4$	-11.5	-	76(b)
16	$[Cu\ (L^2)]$	-8.5	-	76(b)
17	[Ni(L)(DMF)]	-6.6	2.358	77(a)
18	[Mo(dien)O3]	-9.9	6.539	77(b)
19	$[Cu(L)(Phen)_3]^{2+}$	-8.40	0.661	78
20	$[CuCl_3]^-$	-5.2	-	79
21	$\{Mn(H_2L)Cl_2]$	-10.46	-	80(a)
22	[Ni(salen)]	-7.4	-	80(b)
23	[Fe(salen)Cl]	-7.0	-	80(b)
24	$Cu(L)_2]$(**1**)			This work
	6WKP	-10.2	2.134	
	7WRL	-11.9	1.369	
25	$[Ni(L)_2]$(**2**)			This work
	6WKP	-9.5	2.203	
	7WRL	-8.7	2.641	

Table S10. Structure activity relationship (SAR) between the experimental geometries of the bis-Schiff base metal(II)

complexes $[Cu(L)_2]$(**1**) and $[Ni(L)_2]$(**2**) determined by the single crystal X-ray diffraction technique and the theoretical geometries observed upon interactions with HIV-1 protease(PDB ID: 8CI7) and DNA binding protein (PDB ID: 7UV6).

Complexes	Experimental bond lengths (Å)		Docked complexes inside HIV-1 protease and DNA binding protein with bond lengths (Å)			
			PDB ID: 8CI7		PDB ID: 7UV6	
$[Cu(L)_2]$(**1**)	Cu(1)-N(1)	2.023(5)	Cu(1)-N(1)	2.02268	Cu(1)-N(1)	2.02266
	Cu(1)-N(4)	2.028(5)	Cu(1)-N(4)	2.02799	Cu(1)-N(4)	2.02779
	Cu(1)-S(2)	2.2593(18)	Cu(1)-S(2)	2.2596	Cu(1)-S(2)	2.25939
	Cu(1)-S(1)	2.2765(17)	Cu(1)-S(1)	2.27507	Cu(1)-S(1)	2.27588
$[Ni(L)_2]$(**2**)	Ni(1)-N(1)	1.923(11)	Ni(1)-N(1)	1.92239	Ni(1)-N(1)	1.92311
	Ni(1)-S(1)	2.186(3)	Ni(1)-S(1)	2.18647	Ni(1)-S(1)	2.18562
	N(1)-N(2)	1.3976(16)	N(1)-N(2)	1.39738	N(1)-N(2)	1.39778
	C(1)-N(1)	1.3017(17)	C(1)-N(1)	1.30099	C(1)-N(1)	1.30041